Title

Eukaryotic Cell Migration — from Single Cell to Collective Behavior

Author

Tang, Man Ho

Publication Date

2022

UNIVERSITY OF CALIFORNIA SAN DIEGO

Eukaryotic Cell Migration — from Single Cell to Collective Behavior

A dissertation submitted in partial satisfaction of the
requirements for the degree
Doctor of Philosophy

in

Physics (with a specialization in Quantitative Biology)

by

Man-Ho Tang

Committee in charge:

Wouter-Jan Rappel, Chair
Chunhui Du
Alexander Groisman
Elena F Koslover
Bo Li

2022

The dissertation of Man-Ho Tang is approved, and it is acceptable in quality and form for publication on microfilm and electronically.

University of California San Diego

2022

DEDICATION

To my parents, and teachers in my life

who cultivated my curiosity about the world

TABLE OF CONTENTS

LIST OF FIGURES

LIST OF TABLES

ACKNOWLEDGEMENTS

I thank my advisor Wouter-Jan Rappel for his guidance and support throughout my PhD. Wouter leads me into studying the world of a fascinating social amoeba, *Dictyostelium discoideum*, and trains me to become an independent researcher. He has always been a patient and supportive mentor to me.

I also thank Richa Karmakar and Elisabeth Ghabache for teaching me various experimental skills, Yuansheng Cao for theoretical discussions on my research projects. It has been a pleasure to work with former and current members in our research group, including Albert Bae, Haicen Yue, Daniel Lombardo, Aravind Karanam, Timothy Tyree, Dorsa Elmi, Michael Reiss, Arabinda Behera and Mahesh Mulimani.

I appreciate my committee members for their feedback on my research projects. I learned a lot of laboratory techniques, including application of microfluidic devices, from Alex Groisman. I thank Elena Koslover for her advice and interactions we have had about research and teaching. I was a teaching assistant for Chunhui Du's lab class and she helped me develop my teaching skills. I enjoyed the mathematical biology seminar series held by Bo Li which gave me inspirations on my research.

I also thank my friends and roommates — Anamika Argawal, Anchal Gupta, Gene Leung, Jonathan Lam and Joyce Ip, who always have brought joy and laughter along my PhD journey. I am grateful to have shared lots of memorable moments with these friends.

Lastly, I want to thank my parents and sisters for raising me to be a curious learner. Without them, I would not be able to pursue my PhD at UC San Diego.

Chapter 2, in full, is a reprint of the material with minor edits, as it appears in: M.-H. Tang, R. Karmakar, H. Yue, D. Lombardo, A. Karanam, B. A. Camley, A. Groisman, W.-J. Rappel, "Cellular memory in eukaryotic chemotaxis depends on the background chemoattractant concentration", *Physical Review E*, 103 (1), 012402, (2021). The dissertation author was the primary author of this paper.

Chapter 3, in full, is currently being prepared for submission for publication of the material. M.-H. Tang; A. Bae; R. Karmakar; A. Groisman and W.-J. Rappel, “Motion-induced topological defect initiates collective signaling vortex state”. The dissertation author was the primary author of this paper.

Chapter 4, in full, is currently being prepared for submission for publication of the material. M.-H. Tang; S. Ranamukhaarachchi; A. Walker; S. Fraley and W.-J. Rappel, “Matrix degradation determines morphologies and migration modes of cancer cells in dense extracellular matrix”. The dissertation author was the primary author of this paper.

VITA

2015	B. Sc. in Physics, The Chinese University of Hong Kong
2016 - 2017	qBio Research Fellow, University of California San Diego
2018 - 2022	Lab TA Coordinator (PHYS 2CL), Department of Physics, University of California San Diego
2019	M. S. in Physics, University of California San Diego
2022	Ph. D. in Physics (with a Specialization in Quantitative Biology), University of California San Diego

ABSTRACT OF THE DISSERTATION

Eukaryotic Cell Migration — from Single Cell to Collective Behavior

by

Man-Ho Tang

Doctor of Philosophy in Physics (with a specialization in Quantitative Biology)

University of California San Diego, 2022

Wouter-Jan Rappel, Chair

Cell migration is the movement of a single cell or group of cells, usually in response to various environmental cues. It is crucial in many biological processes, including morphogenesis, immune response and metastasis of cancer cells. This dissertation studies eukaryotic cell migration from single cell level to collective behavior using both experiments and theoretical models.

In Chapter 2, we study single cell migration of the social amoeba *Dictyostelium discoideum* and investigate the effect of background chemoattractant concentration on cellular memory in eukaryotic chemotaxis. Our results suggest that aggregation of *Dictyostelium* cells can be facilitated by a rising level of chemoattractant during its developmental program.

In Chapter 3, we study the collective behavior of the social amoeba *Dictyostelium discoideum* during its multicellular mound stage. We find tight correlation between the traction force, signaling activity and cell velocity in the mound, all showing oscillations in their magnitude with the same period. With our mathematical model and perturbation experiments, we show that collective cell motion is crucial in setting up a persistent signaling vortex state within the mound.

In Chapter 4, we study the collective behavior of breast cancer cells (MDA-MB-231) and liver cancer cells (SK-HEP-1) during their proliferation in dense extracellular matrices (ECMs). We find the formation of two distinct morphologies and migration modes, namely rotational spheroids and invasive networks. Our experimental and numerical results show that the localization of matrix-degrading enzymes is a key factor in distinguishing formation of the distinct structures and migration modes.

Chapter 1

Introduction

Cell migration is the movement of a single cell or groups of cells that usually occurs as a response to various environmental cues. It is an important process that affects the functioning of many biological systems. For example, during the egg-chamber development of *Drosophila*, a cluster of cells (known as border cells) detaches from the epithelium and migrates through the surrounding nurse cells in order to reach the oocyte and enable fertilization. Mutants with defects in this border-cell migration process result in production of numerous unfertilized eggs. [1]. In wound healing, epithelial cells migrate collectively as a coherent sheet to the site of injury to restore the epithelial barrier. When the levels of certain migration-stimulating chemicals are too high, migration will happen in an uncontrolled way, leading to the detrimental effect of scattering cells in the epithelial sheets. [2]. For cancer, which is the second-highest leading cause of death in the US in year 2020 [3], metastasis is the life-threatening stage during which tumor cells migrate into the blood or lymph vessels and invade the rest of the body. Numerous studies have been and are still being conducted to study how cancer cells adapt to migrate in different microenvironments [4]. Learning the principles about cell migration is essential to a deep understanding of the above biological phenomena.

A wide variety of cues is known to influence and direct cell migration, including diffusible chemical molecules (chemotaxis), mechanical properties of a surface (durotaxis), electric fields (electrotaxis), light sources (phototaxis) and heat sources (thermotaxis). In a recent review [5], a framework consisting of four principles — the generation, sensing, transmission and execution of the signals — are summarized for cell migration. For all environmental cues, cells need to process information from the signals and generate mechanical movement in accordance.

Traditionally, modes of migration have been classified according to the morphology of the cells. For individual cells moving in a 3D extracellular matrix, the two main categories are mesenchymal and amoeboid modes. [6]. In the mesenchymal migration mode, the crawling movement of cells can be described by a four-step cycle [7]. First, the cell creates a protrusion at the leading edge. For example, lamellipodia are formed by actin polymerization in elongated cells including human HL60 neutrophil-like cells. Then, the cell generates focal adhesions with the substrate by connecting the extracellular matrix to its cytoskeleton. By pulling from the front and contracting at the back, the cell body can be moved forward. Finally, the old adhesions are detached and allow turnover of intracellular materials to form new adhesions. In the amoeboid migration mode, cell can move by forming blebs which are generated by the intracellular hydrostatic pressure. The migration of zebrafish primodial germ cells is an example that relies heavily on blebbing [8]. The blebbing process involves local cortex-membrane detachment to initiate the bleb, followed by pressure-driven cell body expansion into the bleb, resulting in net forward movement. Many cells, including cancer cells, are known to have plasticity to switch between different modes of migration to select the most efficient mode to navigate through the complex extracellular matrix.

The social amoeba *Dictyostelium discoideum* has been a popular model organism for studying cell migration. During its vegetative stage, *Dictyostelium* cells are solitary and feed on bacteria. They are able to chemotactically follow the bacteria by sensing the folic acid secreted by them. Upon starvation, the *Dictyostelium* cells enter a developmental program that involves a self-organized aggregation process. First, they start to secrete and relay cAMP, which is a chemoattractant to the cells. When the resulting cAMP waves propagate through the population of *Dictyostelium* cells, the cells begin to move collectively as streams and form multicellular aggregates, so-called mounds. Subsequently, the mound will develop into a slug during which cells start to differentiate into two types of cell — pre-stalk and pre-spore cells. In the slug, *Dictyostelium* cells continue to move collectively and can travel towards a light source and can respond to pH and temperature gradients [9–11]. When the slug finds a suitable location, culmination of the fruiting body begins where stalk cells will rise to support spore cells. Finally, when the outside environmental condition becomes favorable, the spores can be dispersed and spawn into new feeding cells, completing the life cycle. *Dictyostelium* cells are known to adapt how they move according to the physical environment they are in — extending F-actin-driven pseudopods on smooth surface, creating blebs in mechanically constrained environment, or even swimming if the opportunity arises [12]. Owning to the many fascinating behaviors demonstrated in its life cycle, *Dictyostelium* cells are used as a model organism not only for chemotaxis and cell motility, but also for pattern formation, cell differentiation, multicellular morphogenesis, phagocytosis, autophagy and social evolution [13].

Many mathematical models have been proposed to describe the chemotactic migration process of *Dictyostelium* cells, capturing features including motility, polarization and directional sensing [14]. For gradient sensing, a class of models is based on the local excitation, global inhibition (LEGI) principle. In this model, occupancy of the chemoattractant receptors triggers production of an activator (fast) and an inhibitor (slow) at different rates to produce a downstream transient response. Many proteins and lipids are involved in this complex signaling process, including G proteins, Ras, PI3K, PTEN and PIP3. [15, 16]. *Dictyostelium* cells are observed to be able to respond to very shallow gradients. Models with signal amplification based on a cell front-back asymmetry and a positive feedback of signal and motion have been proposed [17]. It has been shown that the chemoattractant-dependent polarization involves positive feedback of actin polymerization [18]. Meanwhile, on a population basis, other models have focused on the spatiotemporal patterns that arise during the self-organized aggregation of *Dictyostelium* cells, most commonly by describing the population of cells as an excitable media [19]. Waves patterns observed during the aggregation process, including concentric and spiral waves, can be explained by reaction-diffusion models of cAMP [20].

In Chapter 2, we study the effect of background levels of the chemoattrantant cAMP on single-cell migration of *Dictyostelium* cells. It has been shown that cellular memory is an important feature for the cells to maintain its motion during the negative gradient of cAMP waves [21]. In this chapter, we show with experiments and mathematical modeling that the cellular memory depends on the background chemoattractant concentration. Our results suggest that the rising background level of chemoattractant might facilitate the aggregation process of *Dictyostelium* cells during its developmental program.

In Chapter 3, we investigate the persistent vortex state of the multicellular mound of *Dictyostelium* cells by monitoring the traction force, signaling activity and motion of the cells. In this chapter, we show with experiments and mathematical modeling that collective cell motion is crucial in initiating a specific wave pattern — persistent spiral waves of cAMP within the mound. Furthermore, we show that the size of the aggregate plays a critical role in determining the signaling pattern [22].

In Chapter 4, we study the multicellular morphology and migration modes of cancer cells in dense extracellular matrices (ECMs). When single breast cancer cells proliferate in dense ECM, two distinct structures and migration modes, namely rotational spheroids and invasive networks, are observed. Using experiments and mathematical modeling, we show that the spatial distribution of the matrix-degrading enzymes released by the cells is a key factor in determining the morphology and migration mode of the cancer cells.

I carried out theoretical and modeling work in Chapter 2-4, data analysis in Chapter 2-3 and experiments in Chapter 2.

Chapter 2

Cellular Memory in Eukaryotic Chemotaxis Depends on the Background Chemoattractant Concentration

2.1 Abstract

Cells of the social amoeba *Dictyostelium discoideum* migrate to a source of periodic traveling waves of chemoattractant as part of a self-organized aggregation process. An important part of this process is cellular memory, which enables cells to respond to the front of the wave and ignore the downward gradient in the back of the wave. During this aggregation, the background concentration of the chemoattractant gradually rises. In our microfluidic experiments, we exogenously applied periodic waves of chemoattractant with various background levels. We find that increasing background does not make detection of the wave more difficult, as would be naively expected. Instead, we see that the chemotactic efficiency significantly increases for intermediate values of the background concentration but decreases to almost zero for large values in a switch-like manner. These results are consistent with a computational model that

contains a bistable memory module, along with a non-adaptive component. Within this model, an intermediate background level helps preserve directed migration by keeping the memory activated, but when the background level is higher, the directional stimulus from the wave is no longer sufficient to activate the bistable memory, suppressing directed migration. These results suggest that raising levels of chemoattractant background may facilitate the self-organized aggregation in *Dictyostelium* colonies.

2.2 Introduction

Chemotaxis, the movement of cells guided by chemical gradients, plays an important role in many biological processes including tumor dissemination, wound healing, and embryogenesis [1, 23–25]. One of the most studied chemotaxis model organisms is the social amoeba *Dictyostelium discoideum*. Following starvation, *Dictyostelium* cells secrete a chemoattractant, cAMP, in a periodic fashion [26]. This chemoattractant signal is relayed by neighboring cells resulting in waves that sweep over the cell population with periods that range from 6-10 minutes [26–28]. These waves spontaneously organize themselves in spiral or target waves, leading to large-scale patterns of cell migration and eventually generating aggregation centers that attract tens of thousands of cells. Within the resulting aggregates, cells differentiate, with the majority turning into spore cells.

Multiple aspects of this biological system have been investigated using computational and mathematical modeling [29]. Models have addressed instabilities responsible for large scale migration patterns [30, 31], the coupling between intracellular signaling and morphological changes [32–34], and the topology of signaling pathways responsible for guided motion [16, 35, 36]. Furthermore, models have addressed potential mechanisms of gradient sensing [14, 29] while a number of studies have examined the role of noise in the chemotactic response [37–39].

Several experimental and modeling studies have also addressed the so-called back-of-the-

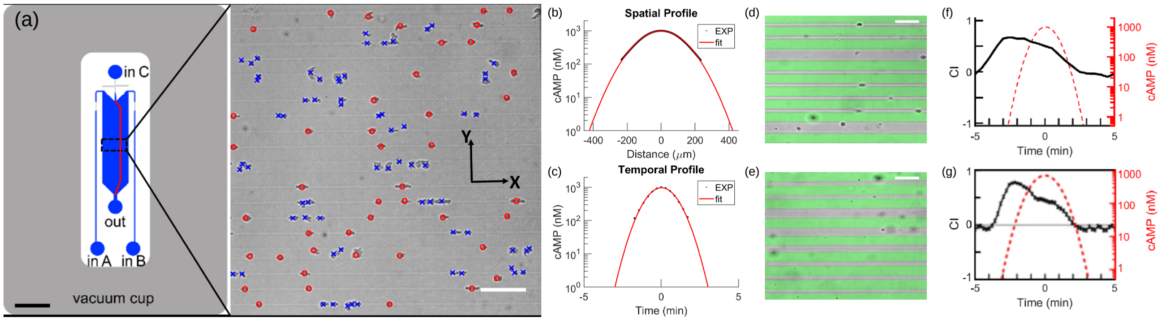

Figure 2.1: Experimental setup using a microfluidic device to create sweeping cAMP waves with adjustable background level. Cells were deposited on a micropatterned substrate and exposed to these waves. The locations of each cell were tracked and their chemotactic performances were quantified. (a): Left: Schematic of the microfluidic wave device, with observation region indicated by black box (Scale bar: 3 mm). Right: Snapshot of cells moving on the micropatterned substrate, with symbols corresponding to cells identified by the machine learning algorithm (red circles: cells used in our analysis; blue X's: excluded cells that are too close to one another; the blurry spots are out-of-focus dirt particles and other irregularities that are not identified as cells by the machine learning algorithm; scale bar: 100 μm). (b-c): Spatial (b) and temporal profile (c) of the cAMP wave, determined from the fluorescent intensity of the dye, and the result of the Gaussian fit. (d-e): Images of the two substrate patterns used in this study, with green highlighting the location of the PEG-gel stripes. The pattern consists of either 4 narrow ($\sim 10\mu$m) and 1 wide ($\sim 25\mu$m) untreated stripes (d) or of 6 variable width stripes, ranging from $\sim 6\mu$m to $\sim 25\mu$m (e). In both patterns, the untreated stripes are separated by 30 μm wide non-adhesive PEG-gel stripes. Scale bar: 50 μm. (f-g): The CI as a function of time for the current experiment using a micropatterned substrate (f) and in a previous study [21], using a non-patterned substrate (g). The results are qualitatively similar, indicating that restricting the cells to 1D stripes does not affect their chemotactic behavior.

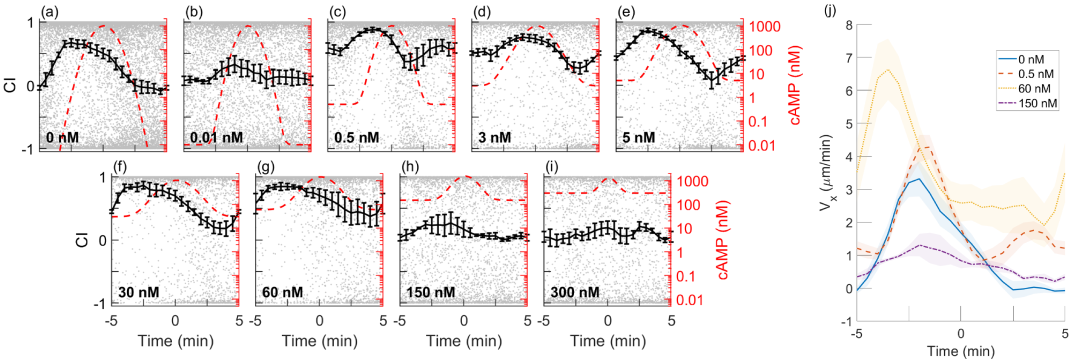

Figure 2.2: (a-i) Experimentally determined average CI as a function of time (measured relative to peak of wave) for different concentrations of background cAMP (0-150nM). In each panel, gray dots represent the CI of individual cells, the black curve is the binned average over N=3-4 different experiments, and the dashed red line is the cAMP concentration of the wave. (j) Average x-component of the velocity of cells for different concentrations of background cAMP. Time is binned in intervals of 0.5 min. Error bars in this figure represent the standard error of the mean obtained using bootstrapping.

wave problem in the chemotactic response to traveling waves [21, 40, 41]. If cells respond only to spatial gradients, they would move forward in the front and backward in the back of the traveling wave, preventing aggregation. These studies have shown that cells exhibit memory, responding directionally to the front but not the back of the wave, enabling them to move efficiently toward the wave source [21, 41]. For wave periods shorter than 10 min, this memory completely prevented reversals of cell migration, whereas for longer periods, cells started reversing their migration direction in the back of the wave [21]. A mathematical model, consisting of an upstream adaptive module and a downstream bistable module, was able to explain the response of cells to periodic waves of chemoattractant [21]. Similar memory phenomena have also been reported in other biological systems, including chemotactic neutrophils [42, 43].

In the experimental studies of memory in *Dictyostelium* chemotaxis, the cAMP waves were applied exogenously, with the cAMP concentration reaching nearly zero in the troughs of the waves. In cAMP waves that are endogenously produced by starving populations of *Dictyostelium*, however, the background cAMP concentration, $\mathrm{cAMP}_{\mathrm{bg}}$, increases from cycle to cycle [44].

This increase occurs because secreted cAMP is not completely removed by phosphodiesterases (PDEs), enzymes that are responsible for the degradation of cAMP and that are also secreted by the cells [45]. Hence, the question how a non-zero $\mathrm{cAMP}_{\mathrm{bg}}$ affects chemotaxis is relevant to the aggregation, sporulation, and survival of *Dictyostelium*. Naively, one would expect a decrease in the cell's ability to migrate towards the source of the wave since the fractional gradient across the cell body, and thus the signal-to-noise ratio, decreases for increasing $\mathrm{cAMP}_{\mathrm{bg}}$[46]. Another possibility is that the cells fully adapt to $\mathrm{cAMP}_{\mathrm{bg}}$, rendering the ability of cells to respond to gradients independent of the background concentration [47].

2.3 Experimental Results

To experimentally study this question, we used a modified version of the microfluidics device from Ref. [21] in which a traveling, bell-shaped wave of cAMP with a peak of 1000 nM periodically sweeps across a gradient channel at a constant speed (Fig. 2.1a; see Appendix A for further details). The fluorescent intensity profile with $\mathrm{cAMP}_{\mathrm{bg}}$=0 was well fitted using a Gaussian (Fig. 2.1b-c and Appendix A) and the resulting wave profile is similar to the one measured for natural waves of cAMP [48, 49]. Importantly, and in contrast to previous studies, the background concentration of cAMP was a variable parameter. Another major modification was that the glass substrate in the gradient channel was micropatterned with $\sim$1.5 μm thick stripes of cell adhesion-blocking polyethylene glycol (PEG) gel. Examples of the two types of micropatterned substrates used in this study are shown in Fig. 2.1d-e. These substrates limit the adhesion and migration of *Dictyostelium* cells to $\sim$6-$\sim$25 μm wide stripes of non-PEG treated glass oriented in the x-direction, along the gradient and perpendicular to the flow. A detailed description of these micropatterned substrates can be found in Ref. [50], where it was shown that cells are nearly exclusively constrained to glass stripes. As a result, cell migration was effectively one-dimensional (1D), either up or down the gradient (positive or negative x-direction), greatly facilitating the collection and analysis of data as compared to 2D chemotaxis on a standard glass substrate.

In our experiments, we exposed cells to repeated waves of cAMP and recorded their movement, excluding the first wave. We used cells of the axenic *Dictyostelium discoideum* strain AX4 that were transformed to express a fusion of GFP to LimE (Δ coil LimE-GFP) and a gene encoding a fusion of RFP to Coronin (LimE GFP/corA RFP) [51]. The cells were grown in submerged shaking culture in HL5 medium (35.5g HL5 powder (Formedium, Norfolk, UK) and 10mL Penicillin-Streptomycin (10,000 U/mL; Gibco, Thermo Fisher Scientific, USA) per liter of DI water) [52]. For starvation, when cells reached their exponential growth phase (3-4 $\times$ 10^6 cells/mL), they were harvested by centrifugation at 3000 rpm for 5 min, resuspended in KN_2/Ca buffer (14.6 mM KH_2PO_4, 5.4 mM Na_2HPO_4, 100 μM $CaCl_2$, pH 6.4), collected by centrifugation, and re-suspended in KN_2/Ca at 10^7 cells/mL. Cells were developed for 5 h with pulses of 50 nM cAMP added every 6 min. Differential interference contrast (DIC) images were taken every 15 s in four fields of view spanning the width of the chemotaxis channel, 2800 μm away from the cAMP inlet, on a spinning-disk confocal Zeiss Axio Observer inverted microscope using a 10X objective and a Roper Cascade QuantEM 512SC camera. Images were captured and analyzed by using Slidebook 6 (Intelligent Imaging Innovations).

Cells were tracked with a custom-made machine-learning algorithm detailed in Appendix B. Only cells that were at least 33 μm from neighboring cells were used in the analysis (marked by red circles in Fig. 2.1a) while cells that were part of clusters were not taken into account (marked by blue crosses in Fig. 2.1a). This algorithm was able to capture more than 90% of single cells, as determined by manual counting. Using cell tracks, we quantified the directional response by computing the chemotactic index CI, defined as ratio between the velocity in the *x* direction and the speed, computed as the difference in the x-position 3 frames prior and 3 frames forward (a 90 s interval): CI=V_x/V. Thus, this quantity ranges from +1 (cells with velocity perfectly aligned to the $+x$ direction), to -1 (cells with velocity perfectly aligned to the $-x$ direction).

We first examined how cells responded to chemoattractant waves with a period of 10 minutes and very low background concentration; $\mathrm{cAMP_{bg}}$=0 and 0.01 nM). This wave period was chosen since it corresponds to the largest period for which the CI in 2D assays remained positive in the back of the wave [21]. The CI for these background concentrations, shown as a black line in Figs. 2.2a and b, computed by averaging over different experiments and over 30s time-intervals, was nearly zero for cells ahead of the wave front, steeply increased to a maximum of $\sim$0.7 as cells were exposed to the wave front, stayed high after the peak of the wave has passed, and gradually decayed to near zero but never became negative. The response for zero background is qualitatively similar to that in 2D *Dictyostelium* chemotaxis assays on plain substrates [21], indicating that constraining the cells to narrow stripes does not change their behavior and that the cellular memory reported in 2D assays is fully manifested in 1D assays as well (Fig. 2.1f-g).

Next, we exposed cells to the same periodic waves but with larger background concentrations ($\mathrm{cAMP_{bg}}$=0.5, 3, 5, 30, and 60 nM) (Fig. 2.2c-g). We found that the average CI improved for these values of $\mathrm{cAMP_{bg}}$: the CI remained much greater than 0 during the entire wave cycle. Furthermore, the CI showed a clear minimum after the peak of the wave has passed and *increased* towards the end of the wave cycle even though $\mathrm{cAMP_{bg}}$ was at its lowest level. For the two largest values of $\mathrm{cAMP_{bg}}$ tested, $\mathrm{cAMP_{bg}}$=150 nM and 300 nM, the CI was reduced and remained close to zero throughout the entire wave cycle (Fig. 2.2h-i). Both the increase in average CI for small values of the background concentration (0.01 to 0.5nM transition) and the decrease in average CI for large values of the background concentration (60 to 150nM transition) were significant ($p < 10^{-4}$, using a z-test). Thus, the background cAMP concentration has a profound effect on the chemotactic response, with intermediate/large values of $\mathrm{cAMP_{bg}}$ enhancing/suppressing the response.

The effect of the background concentration was also evident from the quantification of the x-component of the velocity, V_x. This quantification is shown in Fig. 2.2e where we plot V_x, also averaged over different experiments and over 30s time-intervals, as a function of time

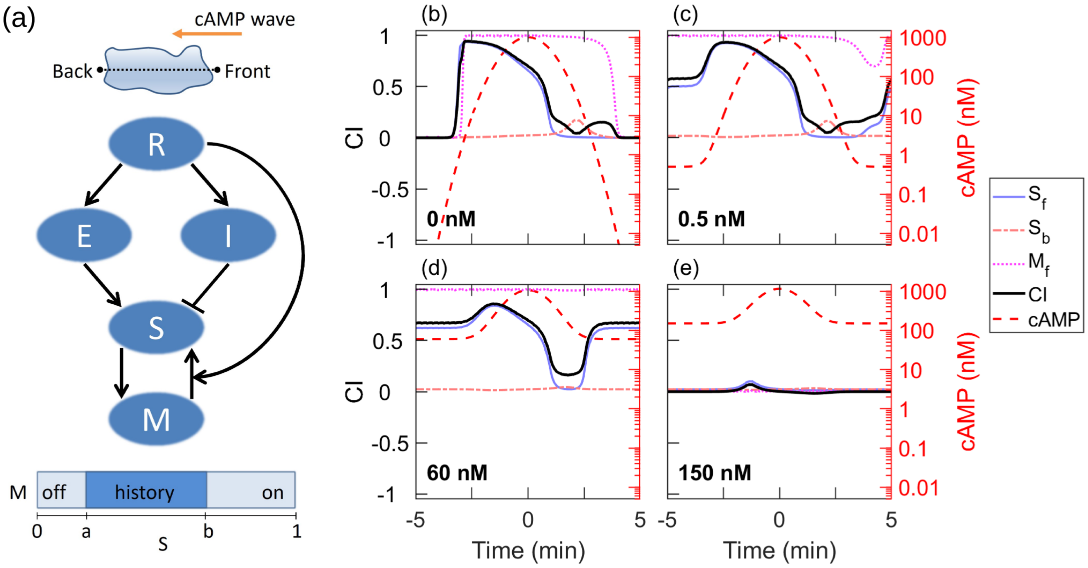

Figure 2.3: (a) Schematic diagram of the chemotactic model, consisting of a receptor R, an activator E, an inhibitor I, a response element S, and a memory component M. Simulations are carried out in a 1D geometry (top drawing). As indicated by the bottom bar, M is bistable, with a low and a high state, determined by parameters a and b. (b-e) Model results for different background cAMP concentrations added to a periodic wave, shown as a dashed red line. The black line represents the CI, the blue (light gray)/red (dash-dotted) line is the response S at the front/back of the cell, and the dotted magenta line corresponds to the memory M at the front.

for different $\mathrm{cAMP_{bg}}$. While this velocity component remained positive or close to zero during the entire cycle for all values of $\mathrm{cAMP_{bg}}$, its maximum value is clearly larger for intermediate values of $\mathrm{cAMP_{bg}}$ than for $\mathrm{cAMP_{bg}}$=0nM. Furthermore, V_x is significantly reduced for the large background concentrations ($\mathrm{cAMP_{bg}}$=150 nM).

2.4 Model Results

To investigate plausible mechanisms for this enhanced cellular memory, we turned to modeling. Specifically, we asked whether the cellular memory model developed by Skoge *et al.* [21] can reproduce the experimental results. This model describes the chemotaxis pathway in terms of abstract variables, although, for some, identification with biochemical components may be possible. Key features of this model are perfect adaptation upon uniform stimulation and cellular memory in gradients [21, 53]. It is schematically shown in Fig. 2.3a and contains an adaptive module, which incorporates an incoherent feedforward Local Excitation Global Inhibition (LEGI) mechanism [16, 35] and consists of a receptor R, an activator E, an inhibitor I and a response element S (Fig. 2.3a). In addition, the model contains a memory module, which is assumed to be bistable such that its component M can be either in a low or high state. The transition between these state is determined by two thresholds, a and b and M feeds back to S. Importantly, this feedback depends on R and this non-adaptive link may be thought of as representing parallel pathways for chemotaxis described in experimental studies [54]. For simplicity, we neglect the detailed morphology of the cell and model it as a 10 μm line with the two endpoints representing the front and back, respectively (Fig. 2.3a). At the front, the model is written as

$$\begin{aligned}
\frac{dR_f}{dt} &= k_R(\mathrm{cAMP}+\mathrm{cAMP}_{\mathrm{bg}})(R_f^{tot}-R_f)-k_{-R}R_f && (2.1)\\
\frac{dE_f}{dt} &= k_E R_f - k_{-E}E_f && (2.2)\\
\frac{dM_f}{dt} &= -k_{Mem}M_f(M_f-M_f^{tot})\left(M_f-M_f^{tot}\frac{b-s_f}{b-a}\right) && (2.3)\\
\frac{dS_f}{dt} &= k_S E_f\frac{S_f^{tot}-S_f}{K_{m1}+S_f^{tot}-S_f}-k_{-S}I\frac{S_f}{K_{m2}+S_f}+k_{S2}M_fR_f\frac{S_f^{tot}-S_f}{K_{m3}+S_f^{tot}-S_f} && (2.4)
\end{aligned}$$

and a similar set of equations applies for the components at the back, labeled with subscript b. The first equation describes the binding/unbinding dynamics of cAMP to the receptor with on and off rates k_R and k_{-R}, respectively. Here, cAMP is the time-varying concentration due to the wave and its dynamics is taken from a Gaussian fit to the wave profile (Fig. 2.1b-c). The second equation models the activator dynamics, parametrized by the activation rate k_E and the degradation rate k_{-E}. The third equation describes the bistable memory module, which has two stable steady states 0 and M_f^{tot}. The output of the model, S, obeys Michaelis-Menten kinetics and is activated with rate k_S by the activator E. It is de-activated with rate k_{-S} by an inhibitor I, which diffuses within the interior of the cell. We will assume that I is uniform throughout the cell, corresponding to a high diffusion rate, and is activated by the average of R between the front and the back $R_{av}=(R_f+R_b)/2$, along with a small basal activity k_{basal}, and can spontaneously degrade with rate k_{-I}:

$$\frac{dI}{dt}=k_I(k_{basal}+R_{av})-k_{-I}I \qquad (2.5)$$

We set the Michaelis constants, K_{m1} and K_{m2}, to be small ($K_{m1},K_{m2}\ll 1$) to achieve near zero-order ultra-sensitivity, which, consistent with experiments, can result in the amplification of shallow external cAMP gradient [55, 56]. The last term in the equation for S_f describes the feedback from the memory module to the activation of S_f, parametrized by the activation rate k_{S2} and Michaelis constant K_{m3}. For simplicity, we will take $M_f^{tot}=M_b^{tot}=S_f^{tot}=S_b^{tot}=R_f^{tot}=$

$R_b^{tot} = 1$. The equations were simulated using an adaptive Runge-Kutta method with variable step size. To prevent the memory from becoming trapped in a fixed point, we reset M_f and M_b every t=15s to δ or $1-\delta$ if their values are smaller than δ or larger $1-\delta$ (δ=0.01).

Model parameters were determined using a fitting procedure (detailed in Appendix C), which minimized a loss function L that compared simulation results (x_{sim}) to experimental results (x_{exp}) with uncertainty σ_{exp}: $L = \sum_{n=1}^{N} |x_{exp} - x_{sim}|/(N\sigma_{exp})$. Here, $N = 56$ with 46 data points chosen from previous experiments using different microfluidic devices [21, 53] and the remaining 10 data points chosen from the current experiments. Details of the previous data points used in the fitting are presented in Appendix C while the new data points consisted of data for cAMP$_{\text{bg}}$ of 0, 0.01, 0.5, 60, and 150nM that were chosen since they represent the three qualitatively distinct responses observed in the experiments. Specifically, in our fitting we required that M_f 2.5 minutes before and 5 minutes after the peak to be either 0, corresponding to a small experimental value of CI, or 1, corresponding to a high CI in the experiments. Simulated annealing was used to find possible global minima, followed by a pattern search to obtain the local minima using the Matlab routine patternsearch. Importantly, the parameter values for the bistable and adaptive module were taken from previous studies [21, 53] and only parameters associated with the memory module (a, b, k_{Mem}, k_{S2} and K_{m3}) were adjusted. The parameter values obtained by our fitting procedure are listed in Table 1 while a fit to previous data is shown in Fig. 2.4a-b.

Simulation results for cAMP$_{\text{bg}}$=0 (Fig. 2.3b) show that the chemotactic response, quantified by CI (computed, following our earlier study [21], as a linear combination of S and M: CI$= 0.1831(M_f - M_b) + 0.8169(S_f - S_b)$ is in qualitative agreement with the experimentally measured CI (cf. Fig. 2.2a). In this case, as the wave approaches the cell, the small difference in cAMP between the front and back is greatly amplified because of the ultra-sensitivity of the response. The resulting large increase in S_f (blue (light gray) line) causes a transition of M_f (dotted magenta line) to the high state. Since S_b (dash-dotted red line) remains low, M_b stays in the low state, and the CI is high (black line). After the wave sweeps over the cell, S_f decreases

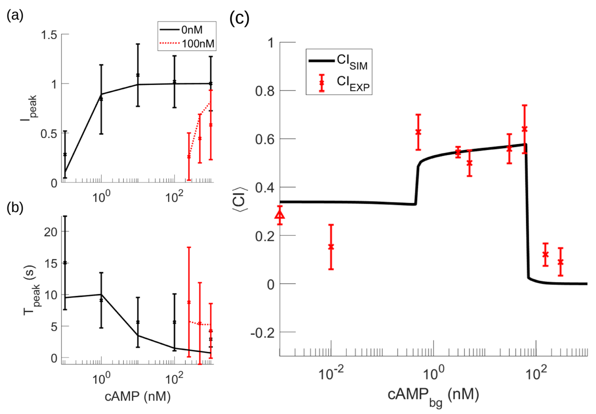

Figure 2.4: (a-b): Comparison between experimental results from Ref. [53] (symbols) and model results. Shown are the maximum change in intensity I_{peak} (a) and its corresponding time T_{peak} (b) as a function of the uniform change in cAMP concentration for two different cAMP pretreatment concentrations. (c): Average CI (red symbols) versus background cAMP concentration.

while M_f remains high for several minutes, resulting in cellular memory and an elevated CI. Eventually, however, the low values of S_f cause a transition of M_f to its low state and the CI decreases to zero (see below and Fig. 2.5).

Intermediate values of $\mathrm{cAMP_{bg}}$ ($\mathrm{cAMP_{bg}}$=0.5-69 nM) result in higher values of S_f, maintaining M_f in a high state for the entire wave period (Fig. 2.3c-d). This increase in S_f is due to the feedback from M_f to S_f, which is, through the non-adaptive link, proportional to the receptor occupancy R_f. Since this occupancy is an increasing function of $\mathrm{cAMP_{bg}}$, the feedback loop between S_f and M_f contributes to a sustained positive CI throughout the entire wave cycle (Fig. 2.3c-d), in agreement with the experimental results. This feedback from high M_f is also responsible for the increase of S_f in the back of the wave (Fig. 2.3c-d). As a result, the CI shows a distinct increase near the end of a cycle, which is, again, consistent with the experimental results.

For $\mathrm{cAMP_{bg}}>69$ nM, both S_f and CI remain close to 0 during the entire cycle, which is consistent with the experimental results for $\mathrm{cAMP_{bg}}$=150 and 300 nM. The reason for this is that the amplification of S_f due to the ultra-sensitivity of the response is reduced for increased values of $\mathrm{cAMP_{bg}}$ (see below and Fig. 2.5). As a result, the value of S_f is not sufficiently large to bring M_f to its high state. Consequently, M_f remains in the low state, leading to a short and weak response of S_f and an overall low CI (Fig. 2.3e). Note that for our parameter values, the dissociation constant for the receptors is $K_d \approx 408$nM. Thus, the absence of a strong chemotactic response for high values of cAMP$_{\mathrm{bg}}$ is not due to receptor saturation but is directly linked to the bistability and the ultra-sensitivity of the pathway.

We also used the modeling results to compute the chemotactic index averaged in time over the entire wave cycle, $\langle \mathrm{CI} \rangle$. The dependence of $\langle \mathrm{CI} \rangle$ on cAMP$_{\mathrm{bg}}$ has three distinct regimes (Fig. 2.4c). For very small values of cAMP$_{\mathrm{bg}}$ (cAMP$_{\mathrm{bg}} < 0.5$ nM) $\langle \mathrm{CI} \rangle$ remains close to its value at cAMP$_{\mathrm{bg}}$=0. For these values of cAMP$_{\mathrm{bg}}$, the memory is only turned on during part of the wave cycle. In contrast, for intermediate values of cAMP$_{\mathrm{bg}}$ (0.5 nM $\leq$ cAMP$_{\mathrm{bg}}$ $\leq$ 69 nM), M_f is in the high state during the entire cycle, resulting in a nearly constant and high $\langle \mathrm{CI} \rangle$. Finally, for cAMP$_{\mathrm{bg}}$ $>$ 69 nM, M_f is always in the low state and $\langle \mathrm{CI} \rangle$ is close to 0. Notably, due to the bistable dynamics of our memory module, the transitions between these regimes are very abrupt and switch-like. To determine whether our experimental data also exhibited this switch-like behavior, we computed the average CI in the experiments. The results are plotted as symbols in Fig. 2.4c and are close to the results of the model (line). Most importantly, $\langle \mathrm{CI} \rangle$ decreases in a switch-like fashion from as much as $\sim$0.6 at cAMP$_{\mathrm{bg}}$=60nM to as little as $\sim$0.1 at cAMP$_{\mathrm{bg}}$=150nM, in agreement with the bistable dynamics of the memory module.

To understand the transition in the model behavior for small values of cAMP$_{\mathrm{bg}}$, shown in Fig. 2.4c, it is useful to examine the response of S_f with $M_f = 1$. For this case, we plot in Fig. 2.5a the steady state solution for S_f as a function of uniform cAMP$_{\mathrm{bg}}$(i.e., in the absence of a wave). S_f increases from 0 to approximately 0.6 as the background cAMP concentration increases. This increase is due to the feedback from M_f to S_f, which is proportional to the receptor occupancy R_f, an increasing function of cAMP$_{\mathrm{bg}}$. The dependence of S_f on cAMP$_{\mathrm{bg}}$ explains why for small values of cAMP$_{\mathrm{bg}}$ the chemotactic index CI reduces to zero following the wave (see Fig. 2.3a and Fig. 2.4c). This is further illustrated in Fig. 2.5b where we plot S_f and M_f for cAMP$_{\mathrm{bg}}$=0.4nM and cAMP$_{\mathrm{bg}}$=0.5nM. For cAMP$_{\mathrm{bg}}$=0.4nM, S_f remains close to the lower

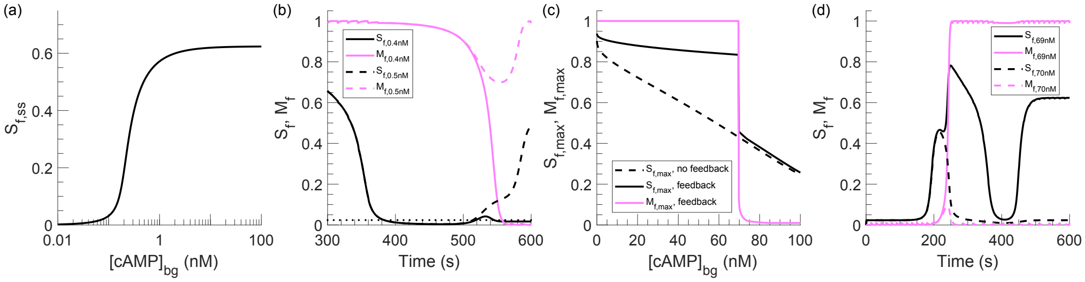

Figure 2.5: A: Steady-state value of S_f as a function of uniform cAMP$_{\text{bg}}$ for the case M_f=1. B: S_f and M_f as a function of time in the full model for a value of cAMP$_{\text{bg}}$ that does (cAMP$_{\text{bg}}$=0.5nM; dashed lines) and does not (cAMP$_{\text{bg}}$=0.4nM; solid lines) result in persistent memory. C: Maximum value of S_f and M_f in a wave as a function of cAMP$_{\text{bg}}$. There is a sharp, switch-like transition at cAMP$_{\text{bg}}$$\approx$69nM. D: Response of the full model for cAMP$_{\text{bg}}$ just below (cAMP$_{\text{bg}}$=69nM; solid lines) and just above (cAMP$_{\text{bg}}$=70nM; dashed lines) the switch-like transition.

threshold of the bi-stable module (indicated by the dotted line), which causes M_f to transition from the high to the low state, resulting in a vanishing CI. For cAMP$_{\text{bg}}$=0.5nM, however, the feedback from M_f results in higher values of S_f such that the memory stays in its high state.

To analyze the switch-like behavior of Fig. 2.5, we can compute the maximum value of S_f in a wave as a function of cAMP$_{\text{bg}}$. The result is plotted in Fig. 2.5c, both for the full model (solid line) and for the case without feedback from M_f, i.e. $k_{S2} = 0$ (dashed line). As a result of the ultra-sensitivity of the equation, the asymmetry in the response of S is much larger than the asymmetry in the external gradient and the receptor occupancy. As is evident from the plot, this amplification of S_f is a decreasing function of cAMP$_{\text{bg}}$. Therefore, above a critical value of cAMP$_{\text{bg}}$, S_f is no longer able to cause a transition of M_f from the low to the high state. For the values of cAMP$_{\text{bg}}$ above the critical value, the CI will thus remain low (see Fig. 4). Furthermore, due to the bi-stability of the memory module, M_f exhibits a switch-like transition at a critical value of cAMP$_{\text{bg}}$ (magenta (light gray) line). This is also shown in Fig. 2.5d where we plot the response of the full model for a value of cAMP$_{\text{bg}}$ just below and just above the critical value. For cAMP$_{\text{bg}}$=70nM, above the critical value, M_f does not transition to the high state and S_f remains close to 0 for the second half of the wave. For cAMP$_{\text{bg}}$=69nM, on the other hand, M_f switches from its low to its high state, which leads to an increased response. After the wave passes, S_f decreases but then increases to ≈0.6 due to the persistent memory at the front.

The switch-like transitions are also clearly visible when examining the phase diagram of the response of the model in the a-b parameter plane (corresponding to the two thresholds in the memory module). Here, we plot the time averaged difference between the memory at the front and back of the cell, $\langle M_f - M_b \rangle$, for different values of a and b using a color scale (Fig. 2.6). Since we take $a \leq b$ we only present one-half of the space. The parameter values corresponding to Table 1 and used in our study are indicated by the symbol. For $\mathrm{cAMP_{bg}}$=0nM (left panel), the sharp transitions between three different regions are clearly visible. In the dark blue regions, corresponding to large values of b, neither the front nor the back memory is activated, resulting in $\langle M_f - M_b \rangle = 0$. For intermediate values of b and small values of a, the memory at the front is permanently activated while $M_b = 0$, which results in $\langle M_f - M_b \rangle = 1$ (yellow region). In the other regions, the front memory is activated only during part of the wave, giving rise to values of $\langle M_f - M_b \rangle$ that are between 0 and 1. Note that our parameters fall within this region of the phase space. For $\mathrm{cAMP_{bg}}$=60nM, the sharp boundary of the yellow region has moved to larger values of a, such that our parameter values now fall within the region in which $\langle M_f - M_b \rangle = 1$ (middle panel). Finally, for $\mathrm{cAMP_{bg}}$=150nM, the yellow region has almost completely disappeared and nearly the entire phase diagram, including our parameter set, correspond to $\langle M_f - M_b \rangle = 0$.

2.5 Summary

In summary, we find that the background concentration of the chemoattractant, $\mathrm{cAMP_{bg}}$, has a profound effect on the cellular memory of chemotaxing *Dictyostelium* cells. For intermediate values of $\mathrm{cAMP_{bg}}$ this memory is greatly enhanced, leading to substantially more efficient chemotaxis under periodic waves of cAMP. It is worth noting that the experimentally estimated value of $\mathrm{cAMP_{bg}}$ during the natural aggregation process of *Dictyostelium* cells is ∼10nM [44].

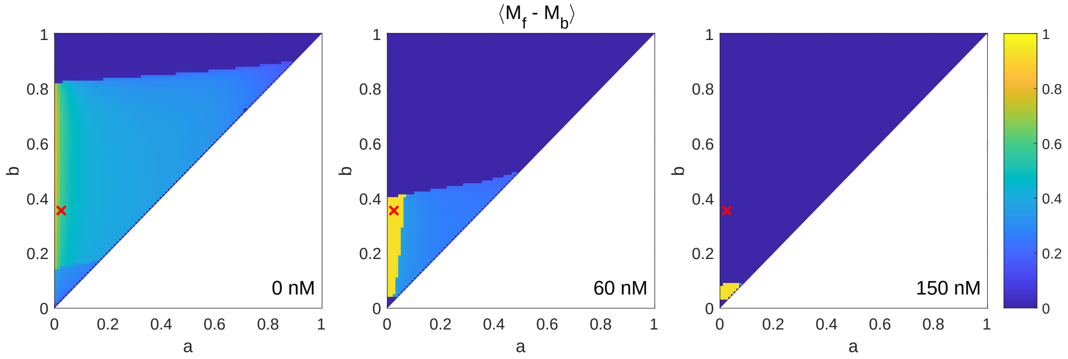

Figure 2.6: Phase diagram in the $a-b$ space quantifying $\langle M_f - M_b \rangle$ for three different values of cAMP$_{\mathrm{bg}}$. Three regions, with sharp transitions, can be identified: $\langle M_f - M_b \rangle = 1$ (yellow regions) for which the front memory is always high while the back memory is always low, $\langle M_f - M_b \rangle = 0$ (dark blue regions) corresponding to low memory at the front and the back, and intermediate values of $\langle M_f - M_b \rangle$ for which the front memory is high during part of the wave. The values of a and b corresponding to our study are marked by a red X.

This value is within the intermediate range, suggesting that aggregation may be facilitated by increased cellular memory due to accumulating cAMP. For larger values of cAMP$_{\mathrm{bg}}$, the chemotactic response and cellular memory are suppressed. Our experimental results, and in particular the switch-like behavior of the average CI, are fully consistent with our mathematical model. Crucial elements of this model are a bistable memory module, which allows cells to ignore the back of the wave, an ultra-sensitive response, responsible for the amplification of the chemoattractant gradient, and a direct, non-adaptive link between input signal and response, which explains the long-lasting memory for intermediate values of cAMP$_{\mathrm{bg}}$. Future work will be required to identify the precise biochemical components that are responsible for the observed behavior.

2.6 Acknowledgements

R.K. and M.-H.T. contributed equally to this work. We acknowledge support from by the National Science Foundation under grant NSF PHY-1915491 (BC), PHY-1411313 (AG), and PHY-1707637 (W.-J.R.).

Chapter 2, in full, is a reprint of the material with minor edits, as it appears in: M.-H. Tang, R. Karmakar, H. Yue, D. Lombardo, A. Karanam, B. A. Camley, A. Groisman, W.-J. Rappel, “Cellular memory in eukaryotic chemotaxis depends on the background chemoattractant concentration”, *Physical Review E*, 103 (1), 012402, (2021). The dissertation author was the primary author of this paper.

Chapter 3

Motion-induced topological defect initiates collective signaling vortex state

3.1 Abstract

Social amoeba *Dictyostelium discoideum* cells use cAMP as a signal for aggregation during its developmental program. In the intermediate stage, isolated multicellular mounds are formed, in which sustained rotational motion of cells and spirals of signaling waves are observed. This rotational motion can last for hours. The mechanisms responsible for these persistent rotations are currently unclear. Here, by using a microfluidic device, traction force microscopy and a strain that expresses a protein reflecting the cell's cytosolic cAMP level, we present the first measurements of the traction force distribution, together with the signaling dynamics and cell motion in the vortex state of the mound. Using experiments and computational modeling, we show that collective cell motion is crucial in regulating the spatiotemporally stable signaling pattern.

3.2 Introduction

When the social amoeba *Dictyostelium discoideum* is starved, hundreds of thousands of cells will migrate in a coordinated fashion to form multicellular aggregates, that eventually become fruiting bodies, containing spore cells. At the beginning of this developmental program, *Dictyostelium* cells start to secrete cyclic adenosine monophosphate (cAMP) to attract other cells. Each cell can sense the external cAMP level and, in response, releases more cAMP into the environment. This cAMP relay system results in the propagation of cAMP waves throughout the cell population. These waves are observed to travel as concentric target waves or rotating spiral waves. As the cells develop, they become chemotactically sensitive and migrate towards the source of cAMP waves, which is achieved by spatial gradient sensing and signal adaptation. Streams of cells then move collectively towards the aggregation centers. As more cells come together, they pile up and three-dimensional mounds are formed. While many studies have focused on the early stages of aggregation, much less is understood about this mound stage.

For example, persistent rotational movement of cells are observed within the mound [57], but it is unclear what its purpose is and what coordinates this movement. It is possible that this rotational motion plays a role in the cell differentiation into pre-stalk and pre-spore cells during the mound stage. This differentiation is crucial proper culmination of a fruiting body. As only spore cells can eventually survive while the stalk cells die, the cell fate of *Dictyostelium* cells poses an interesting yet unsolved question. Understanding more about the rotational mound stage can possibly shed light on this problem.

In the field of active matter, the study of nematics has bloomed over the years and has attracted many theorists and experimentalists to the field. In basic terms, active nematics are elongated self-propelled units that actively consume energy and move in association with their elongation axis. Examples of active nematics include active liquid crystals and microtubule–kinesin mixtures. A common focus of active nematics is how collective behavior emerges from the individual units. The studies of turbulence and topological defects in active nematics have inspired different approaches in studying biological systems, including the alignment of neural stem cells [59] and the signaling dynamics of membrane proteins [60]. As a model organism for collective migration, *Dictyostelium* cells present a good opportunity to understand how topological defects can affect its developmental program via spatial organization of motion and signaling.

In particular, the aforementioned cAMP signaling of *Dictyostelium* cells can be modeled as an excitable media with reaction-diffusion equations, which exhibit target and spiral wave patterns. Distinct from the non-living classic example of excitable media — the Belousov-Zhabotinsky (BZ) chemical reaction, which also displays various wave patterns [61] — the wave dynamics in *Dictyostelium* cells are far more complex. This is due the fact that *Dictyostelium* cells are motile. Furthermore, the specific wave patterns may directly affect survival of the cells. For example, an intrinsic difference between target and spiral waves is that target waves propagate radially outward and then die out, while spiral wave can rotate and propagate indefinitely. Therefore, the latter may facilitate the aggregation of cells and can result in larger mounds.

In this chapter, we address several questions. What is the role of the persistent rotation of cells in the mound? Does it affect the developmental program of the cells? If so, what is the underlying mechanism? Or is it simply a result of cell responding to a rotating cAMP wave?

3.3 Experimental Results

3.3.1 Experimental Setup

To study the coherent rotational state of *Dictyostelium* cells, we used a custom made microfluidic device to flatten and create vertically constrained cell aggregates. To monitor the cellular signaling activity, cells were transformed to express flamindo2-GFP, which is an indicator for cytosolic cAMP levels [62]. For detecting the mechanical forces generated by the cells in the rotational state, cell mounds were plated on a thin elastic silicone substrate coated with fluorescent beads for traction force microscopy (TFM). In addition to expressing flamindo2, cellulose synthase null (dcsA-) cells were used in order to properly observe the traction force.

In our experiments, cells were grown in shaking HL5 medium (35.5g HL5 powder (Formedium, Norfolk, UK) with 10mL Penicillin-Streptomycin (10,000 Units/mL Penicillin, 10,000 μg/mL Streptomycin, Gibco, Thermo Fisher Scientific, USA) and 200 μL Geneticin (50mg/mL active Geneticin, Gibco, Thermo Fisher Scientific, USA) per 1 liter of Milli-Q water. For starvation, cells in exponential growth phase (2-4 $\times$ 10^6 cells/mL) were collected by centrifugation at 400g for 4 min then resuspended in KN_2/Ca buffer (14.6 mM KH_2PO_4, 5.4 mM Na_2HPO_4, 100 μM $CaCl_2$, pH 6.4). This washing process was done twice more to completely remove the growth medium. After the final wash, 150 μL of total 1.7 $\times$ 10^7 cells were transferred onto a 35mm agar plate (2% agar, 50% KN_2/Ca buffer and $50\% ddH_2O$). With its lid off, the cell plate was placed in a biosafety cabinet with laminar flow to allow excess liquid to evaporate. About 20 minutes later, the lid was put back and further development was stalled by refrigerating the cells overnight at 4-8°C. In the following day, development was resumed by placing the cell plate at room temperature 22°C for 6-8 hours until when tight mounds were observed. These cell aggregates were harvested by pipetting 2mL of buffer up and down the agar surface, followed by repeated pipetting and vortexing to obtain a homogeneous culture. Finally, 150 μL of cells were plated onto the silicone substrate and allowed to settle on it for 10 minutes. Meanwhile, the microfluidic device was plasma-treated for about 8 seconds to make the PDMS surface hydrophilic and reactive for enhanced wetting and bonding to the substrate. The microfluidic device was then placed on top of the cells, and a slight suction (roughly 10 kPa below atmospheric pressure) was applied to the vacuum cup to seal the device onto the substrate and to keep the height confined to around 8 microns (about the size of the cell) allowing formation of monolayer aggregates. Imaging of the flamindo2-GFP dcsA- aggregates was done using an inverted spinning-disc confocal microscope (20X/0.8 air objective, Zeiss and Intelligent Imaging

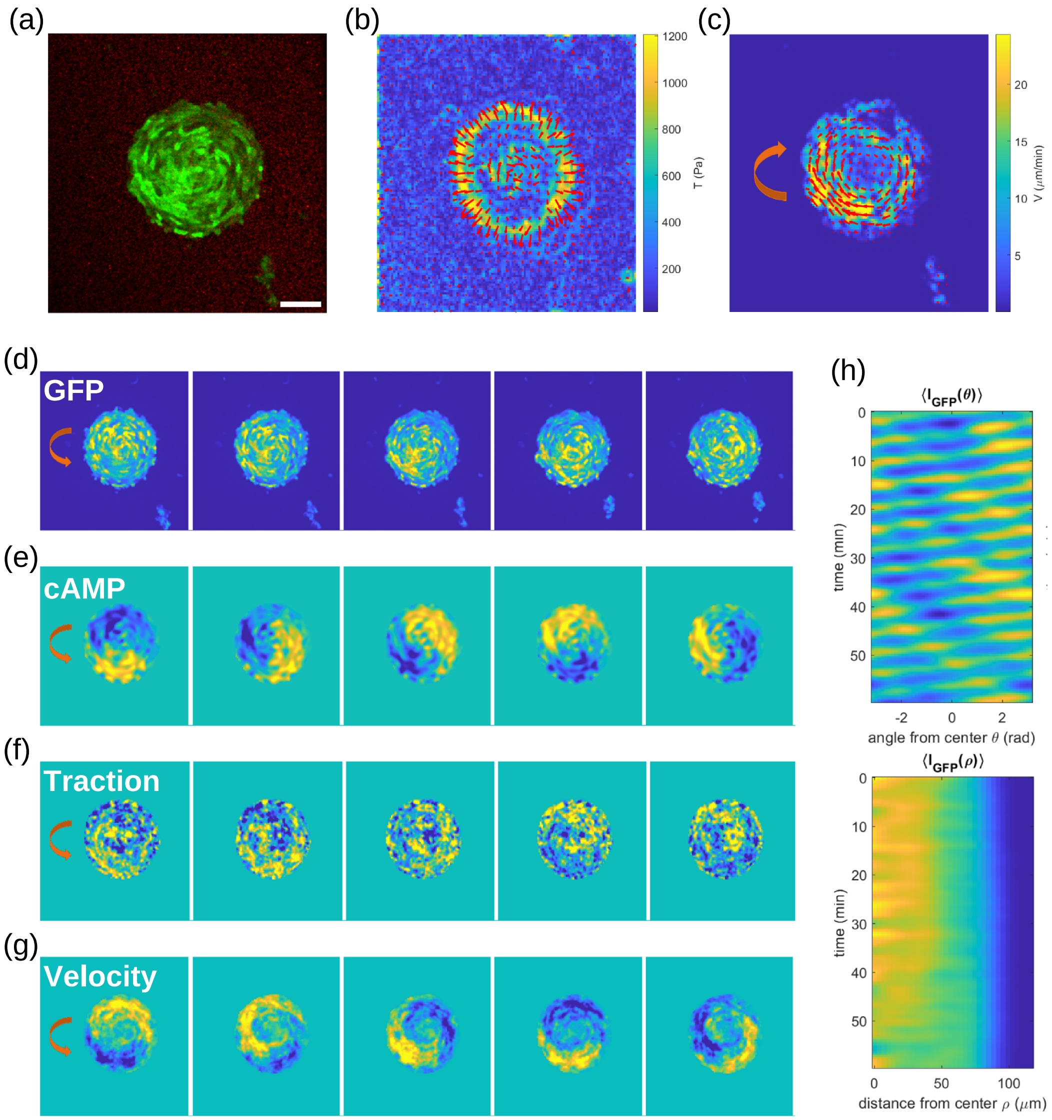

Figure 3.1: Experimental setup using a microfludic device to create vertically constrained aggregates with measurements of cyctosolic cAMP level, traction force and cell velocity. Rotational waves were observed in these measured quantities. (a): Experimental image showing flamindo2 intensity (GFP) of a quasi-2D aggregate deposited on a deformable silicone substrate coated with fluorescent beads (RFP). The cytosolic cAMP level is inversely proportional to the GFP fluorescence intensity. Scale bar: 50 μm. (b-c): Traction force (b) and cell velocity (c) fields of the aggregate. Red arrows represent direction and magnitude of the vector fields. (d-g): Time series of the (d) raw and (e) inverse bandpass-filtered GFP images revealing a rotating cAMP wave (counter clockwise); similar waves can be seen in the time series of bandpass-filtered (f) traction force and (g) cell velocity, with 48 s interval between consecutive images. (h): Kymograph of GFP intensity averaged over [left] angle and [right] distance from center of aggregate. Dark bands in the angle kymograph showing the rotating cAMP wave, which persisted over an hour.

Innovation). Every 24-30 s, images in GFP and RFP channels were captured (Fig. 3.1a). In each capture, the built-in autofocus function in Slidebook 6 (Intelligent Imaging Innovation) was used on RFP channel to find the best focused plane of the fluorescent beads, which corresponded to the bottom of the cells. At the end of each experiment, reference images of the beads were obtained after the cell aggregates were dissolved with a 1% solution of Triton X-100.

3.3.2 Traction force and cell velocity calculations

Displacement maps of the fluorescent beads between the in-focus images and the reference image were found using PIVlab [63]. These displacement maps were then converted to traction force maps (Fig. 3.1b) using the Fourier method presented in [64]. It is worth noting that this method assumed the absence of normal stresses, which was not the case in our system since we had a ceiling that confined the cells by pushing them down, and consequently, the cells would push down on the substrate. However, as the substrates we used were relatively thin (about 5 μm thick), the artifacts introduced by ignoring normal displacements or stresses were negligible [65].

Cell velocity fields (Fig. 3.1c) were estimated using MATLAB Optical Flow Farneback method using the GFP images. The resulting velocities were compared to a set of manually tracked data and found to be in good agreement. Times series of GFP images (Fig. 3.1d-e) revealed a rotating cAMP wave propagating (counter clockwise) within the cell aggregate, which was in opposite direction of the cell motion (clockwise in Fig. 3.1c). This rotating cAMP wave was clear when we examined the angle kymograph (Fig. 3.1h). By fitting straight lines to the dark bands (see appendix.B.1), the period of the rotating cAMP wave can be inferred to be about 4.3 min. Oscillations with the same period were also observed in the magnitudes of traction force and cell velocity (Fig. 3.1f-g).

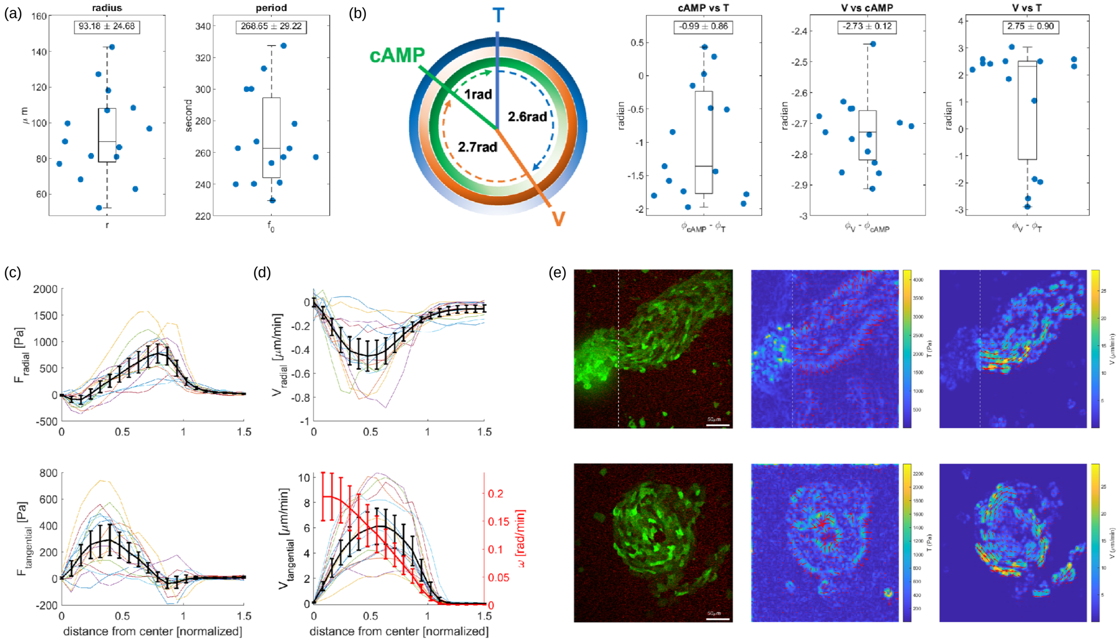

Figure 3.2: Experimental data quantification of multiple aggregates, including the sizes, signaling periods, cytosolic cAMP levels, traction forces and cell velocities. (a): Quantification of sizes and oscillation periods of $N_a = 15$ aggregates in the vortex state. In the boxplots, the [100, 75, 50, 25, 0]th percentile are marked, with the average and standard deviation shown at the top. (b): Phase relationships between traction force (T), cell velocity (V) and cytosolic cAMP level (cAMP). (c-d): Representative spatial profile of the radial and tangential components of (c) traction force and (d) cell velocity as a function of normalized distance from the center of the aggregate. Black line shows the mean values and errorbars represent the standard deviation. Red line shows the angular velocity. Sign conventions are (radial, +: away from center, -: towards center) and (tangential, +: along rotation direction, -:opposite to rotation direction). (e): Traction force and velocity maps of aggregates with different morphology [upper: stream, lower: annulus] where traction forces were always pointing normally outward at the aggregate boundary, and pointing along the cell migration direction inside the aggregate. White dotted lines in upper panels separate ceiling-free region (left) and vertically constrained region (right).

3.3.3 Results

For further quantification, we considered N = 15 aggregates in experiments done on 11 different days. The average radius of the aggregates was $93 \pm 25 \mu m$ (average ± s.d.) consisting of about 100-700 cells (Fig. 3.2a). The period of oscillations was $4.5 \pm 0.5 min$, consistent with reported values in other studies [66]. Shapiro-Wilk tests were performed on the radius (p = 0.9963) and period (p = 0.1925) distribution and it did not show significant departure from the normality ($\alpha = 0.05$). Fig. 3.2b shows the temporal phase relationship between traction force, cell velocity and cytosolic cAMP level. The phase difference was calculated by considering the cross-correlation between a pair of quantities (see appendix B.2).

It can be seen that the cell velocity reached a maximum during the rising phase of the cAMP level, which is expected due to the positive cAMP gradient, in agreement with previous studies [21, 67]. Also, it is interesting to see that the traction force and cell velocity were roughly anti-phase, suggesting that cells exerted the least force on the substrate while they were moving the fastest. We then looked at the spatial profile of traction forces and cell velocities as a function of distance (normalized by the radius of the aggregate) from the center of the aggregate (Fig. 3.2c-d). The average radial movement of the cells was limited (about one-tenth) compared to the tangential movement which was along the direction of rotation. This was expected as any net radial movement would correspond to a change in size of the aggregate, which was possible only if cells were joining or leaving the aggregate (rare), or if they were migrating into the z-direction which was restricted since the aggregates were vertically constrained. The tangential velocity peaked at roughly half the radius with an average value of $6 \mu m/min$. The angular velocity was $\sim 0.2 rad/min$ at the center and gradually decreased as it went further away from the center, corroborating the experimental result in [57]. For traction force, surprisingly the cells exerted mostly a radially outward force on the substrate near the edge of the aggregate with average maximum magnitude of 700 Pa, which was more than double of the tangential component (300 Pa). In its natural developmental program, groups of *Dictyostelium* cells also exhibit other morphologies, including annuli and streams of cells. We occasionally observed these morphologies in our experiments (Fig. 3.2e), and found that a large traction force always existed near the boundary of the aggregates and always pointed normally outward from the aggregate body. Similar results were also observed in other studies [68], but it is unclear what caused this boundary force.

3.4 Model Results

3.4.1 Model Setup

To investigate the underlying mechanisms for the relationship between traction force, cell velocity and cell signaling, as well as the origin of the observed traction force pattern, we developed a 2D grid-based computational Cellular Potts Model (CPM) with an excitable cAMP signaling module incorporated with cell motility.

The Cellular Potts Model has been used as a computational model to study cell and tissue. In its earliest application, it was used to simulate cell sorting by assuming differential adhesion between different cell types [69]. CPM was adapted from the large-Q Potts model which is a generalization of the Ising model used by physicists to study interacting spins on a crystalline lattice [70]. Over the years, extensions have been incorporated into the CPM to study a wide variety of biological phenomena, including morphogenesis [71], tissue growth [72], cell differentiation [73] and would healing [74].

In CPM, each lattice site is assigned with a label (σ) which defines whether it is part of a cell (e.g. σ_1 for cell 1, σ_2 for cell 2) or other materials (e.g. σ_m represents surrounding medium). The cell behavior is determined by the energy of the system, the Hamiltonian (H), which can consist of various energy terms depending on the biological phenomena we are trying to model. The CPM evolves by minimizing the Hamiltonian of the system stochastically using a Metropolis algorithm [75]. In each simulation step, a lattice site m and a neighboring site n

are randomly picked as an attempt to copy the label of site m to site n. The energy difference $\Delta H = H_{n\to m} - H_{current}$ is calculated. If $\Delta H \leq 0$, the cell label of site m would be copied to site n. If $\Delta H > 0$, the copy would take place with a probability of $e^{-\Delta H/T}$, where T is the simulation temperature.

In our model, the Hamiltonian of the simulated system consists of four terms: contact energy, cell size constraint, actin polarization and chemotaxis.

$$\begin{aligned}
H &= H_{contact} + H_{area} + H_{polarization} + H_{chemotaxis} && (3.1)\\
H_{contact} &= \sum_{i,j \text{ neighbors}} J_{\tau(\sigma_i),\tau(\sigma_j)}(1-\delta_{\sigma_i,\sigma_j}) && (3.2)\\
H_{area} &= \sum_n \lambda_a (a(\sigma_n) - A)^2 && (3.3)\\
H_{polarization} &= -\lambda_p \vec{P} \cdot \sum_{i,j\in\sigma} \vec{r}_{ij} && (3.4)\\
H_{chemotaxis} &= -\lambda_c \theta(r_c - r) \nabla S \cdot \sum_{i,j\in\sigma} \vec{r}_{ij} && (3.5)
\end{aligned}$$

The first two terms are conventionally used to model contact energy (e.g. cell-cell adhesion and cell-medium interfacial tension) and to account for the energy cost for a cell to deviate from its optimal size. For contact energy, the coupling strength (J) in Eq. 3.2 depends on the types ($\tau(\sigma)$) of interacting lattice sites, where $J_{c,c}$ represents cell-cell adhesion and $J_{c,m}$ represents cell-medium interfacial tension. The kronecker delta $\delta_{\sigma_i,\sigma_j}$ is 1 if the two interacting cell labels ($\sigma_i = \sigma_j$) are the same, while it is 0 if the cell labels ($\sigma_i \neq \sigma_j$) are different. Thus contact energy is only non-zero between lattice sites with different cell labels but not within the same cell. For the cell size constraint, A represents the target area and $a(\sigma_i)$ is the area of the cell with label i. This quadratic term models the energy penalty when the cell size deviates from the optimal size with a strength λ_a, resembling the elasticity of a cell membrane.

In addition, we have two extra terms in the Hamiltonian representing the polarization energy and the chemotaxis energy. The polarization energy enables our simulated cell to set up a polarity (e.g. front-back asymmetry) for directed cell migration. The importance of cell polarity in both single cell and collective cell migration has been experimentally widely studied with various cell types [76, 77]. In our model, the polarization vector (P) is governed by

$$\frac{dP_x}{dt} = k_+ \frac{v_x}{|v|}(1 - |P|) - k_- P_x \tag{3.6}$$

$$\frac{dP_y}{dt} = k_+ \frac{v_y}{|v|}(1 - |P|) - k_- P_y \tag{3.7}$$

The above equations describe a positive feedback between cell motion (v) and the polarization vector (P), enabling the simulated cell to have persistent motion with a memory depending on the rate constants (k_+ and k_-). This mimics the well-documented positive feedback between actin polymerization and motion of cells [78, 79].

The chemotaxis energy encourages our simulated cell to move along the positive gradient of cAMP. This imitates the ability of *Dictyostelium* cells to sense and migrate in response to cAMP [55]. The equations for the cAMP (S) signaling dynamics are

$$\frac{dS}{dt} = D\nabla^2 S + \alpha_0 - JS + \rho\theta(g - g_c) \tag{3.8}$$

$$I = A\log_{10}(1 + \bar{S}/K) \tag{3.9}$$

$$\frac{dg}{dt} = -k_g g(g-1)(g-a) - k_r r + I \tag{3.10}$$

$$\frac{dr}{dt} = (g - r)/\tau \tag{3.11}$$

Here, the right hand side of Eq. 3.8 describes the diffusion, basal production, degradation and active production of cAMP. Eq. 3.9 models the logarithm sensing of cAMP, while Eq. 3.10 and Eq. 3.11 are the FitzHugh–Nagumo equations [80] corresponding to the activator (g) and repressor (r) dynamics of an excitable media.

Finally, to simulate traction forces, we used a theoretically simple approach that assumes that forces can be derived from the negative gradient of the Hamiltonian of the system (Eq. 3.12).

$$\vec{F} = -\nabla H \tag{3.12}$$

This approach was shown to resemble real forces measured experimentally in a previous study [81].

3.4.2 Numerical Results

Fig. 3.3a shows a simulated aggregate with N=100 cells rotating clockwise while the cAMP waves propagated in the opposite direction (Fig. 3.3b), as observed experimentally. We then ran the simulations multiple times using a distribution of aggregate sizes. The representative spatial profile of simulated traction forces and cell velocities qualitatively matched well with our experimental results (Fig. 3.3c-d). Specifically, the tangential force and velocity had the same direction and peaked at approximately half of the aggregate radius. In addition, the radial force pointed outward near the edge of the aggregate, and the radial velocity was very small compared to the tangential velocity. There were still some quantitative differences, a major one being that the simulated radial force was much smaller than the tangential force, as opposed to the experimental results. This discrepancy was possibly because our simulated traction force only accounted for local interaction between the cells, while in experiment the aggregate might be under pressure or a compression force that can be transmitted across the aggregate. In addition, the relative strength of the radial force is likely to depend on the parameters chosen in the simulation. Future work should explore this parameter space. Nevertheless, despite its simplicity, the model is able to qualitatively capture many experimentally observed features of the rotating aggregate.

Next, we perturbed our model in order to gain insights into the system. Specifically, we changed the size of the aggregate r and the refractory time τ of the repressor. We observed that the number of cAMP spiral arms increases linearly with the aggregate size (Fig. 3.3e). In addition,

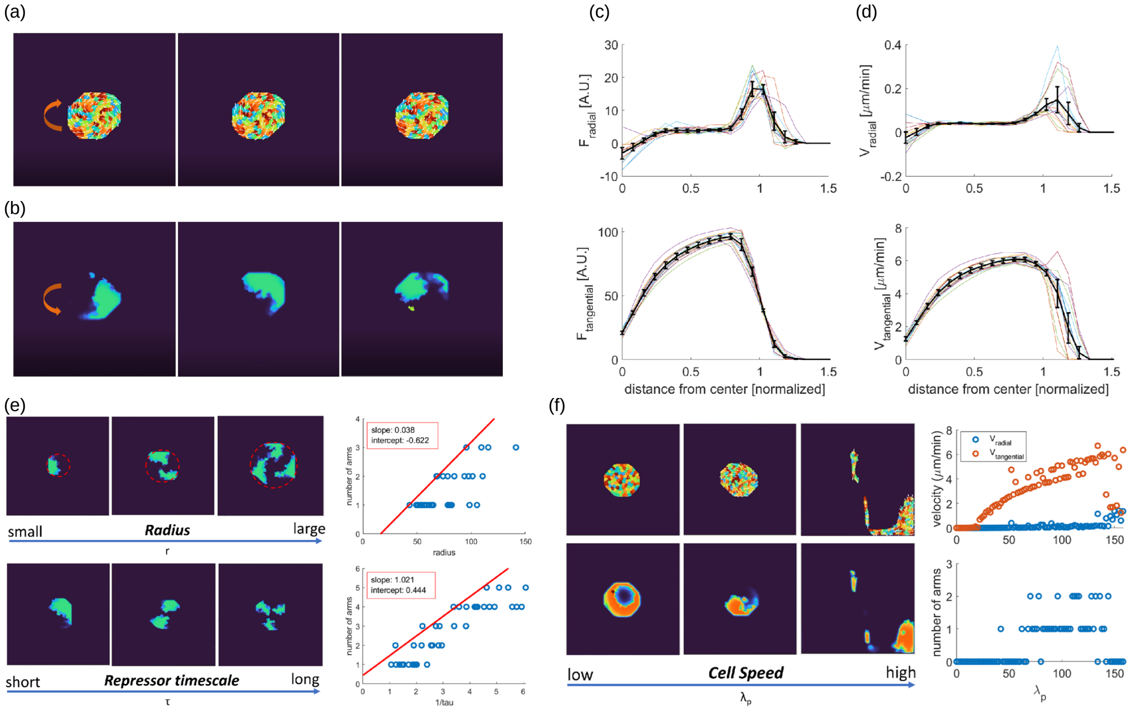

Figure 3.3: Simulation results of aggregates showing rotational motion and signaling. Spatial distribution of simulated traction force and cell velocity resembled the experimental results. Number of spiral arms of the cAMP waves depended on the aggregate size, repressor timescale and cell speed. (a): Simulated aggregates with N=100 cells individually coded with artificial colors for visualization. White arrows indicate the polarization vectors of individual cells. Cells were collectively rotating in clockwise direction. (b): cAMP (S) levels of the simulated aggregates shown in (a) with a rotational wave in counter clockwise direction. (c-d): Representative spatial profiles of simulated (c) traction force and (d) cell velocity as similarly quantified as in Fig. 3.2c-d. (e) Number of rotating arms, n, as a function of the radius of aggregate, r, and the repressor time scale, τ. (f): Snapshots of cell motion (upper row), and signaling (lower row) for different values of the strength of polarization, λ_p. Upper right panel: velocity as a function of λ_p, lower right panel: number of spiral arms as a function of λ_p.

we found that the n is approximately linearly with the inverse of τ (Fig. 3.3e). This finding can be understood if we assume that the cAMP propagation speed is v_0, in which case the number of spiral arms can be approximated by

$$n = \frac{2\pi r^*}{v_0 \tau} \tag{3.13}$$

where r^* is the effective radius of the aggregate. This means that doubling the number of spiral arms would require a doubling of the aggregate radius. Consistent with this, in our experiments, the radius of the smallest aggregate that showed a one-arm rotational wave was about 52 μm, and the smallest one showing two-arm waves was 100 μm. Limited by the field of view in our experimental settings, we did not observe larger aggregate that in principle could exhibit rotational waves with more arms. A previous study [82] has documented rotational optical density waves consisting of up to five arms in *Dictyostelium* cell mound. In their work, FitzHugh-Nagumo equations were also used to study the formation of multiarmed spirals. In comparison, our current model also incorporates cell motility which allows us to study the effect of cell motion on the cAMP spiral dynamics.

Second, even when we removed the cAMP signaling module, our simulated cells could still establish coherent rotation as an aggregate. Hence, according to our models, chemotaxis was not required for the coherent rotation of cells. Instead, cell motility and strong cell-cell adhesion were the key components. This is consistent previous studies in which aggregates of a non-signaling strain were found to still be able to manifest coherent rotations [57, 83].

Lastly, we investigated how cell motion might affect the cAMP signaling pattern. Cell velocity was not explicitly defined in our model. However, due to the polarization energy term (Eq.3.4), cell velocity was indirectly affected by the strength of polarization, λ_p. Hence, by changing λ_p, we can effectively perturb cell velocity. Our simulation results showed that the

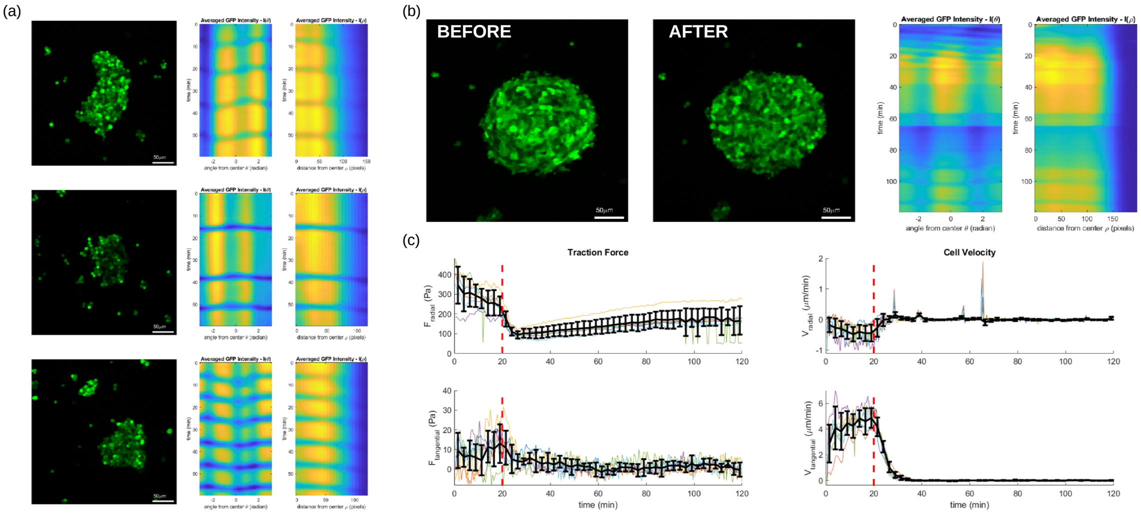

Figure 3.4: Perturbation experiments using LatB revealed changes in signaling wave patterns, from spiral waves to target waves, when cell motion was impeded. (a): Three different aggregates treated with LatB exhibiting target cAMP waves as shown in the kymographs. (b): Rotating aggregate before (t = 15 mins) and after (t = 30 mins) treated with Lat B (t ≈ 20 mins). The cAMP waves changed from rotating (before 20 mins) to target waves (after 80 mins). (c): Time series of traction force and cell velocity averaged over 6 aggregates in the same experiment. Upon LatB treatment, radial force significantly dropped to roughly one-third while the tangential force and cell velocities dropped close to zero. Red dotted line indicates the time when LatB reached the aggregates.

cAMP signaling patterns significantly changed for aggregates with different cell velocities (Fig. 3.3f). At low λ_p, no coherent cell rotation was observed (zero tangential velocity) and only target wave patterns were seen. At intermediate λ_p, corresponding to the experimental regime, cells established coherent rotation and persistent cAMP waves propagating in opposite direction. Lastly, at very high λ_p, cell velocity was so high that the aggregate would separate into smaller groups of cells and migrate translationally. In this case, cAMP waves were only sporadically initiated and short-lived as it propagated through the smaller aggregate, resembling target waves observed in streaming cells.

3.5 Model Verification and Perturbation Experiments

In order to check our model predictions that cell motion regulates cAMP signaling pattern, we decided to experimentally perturb cell motion. For our *Dictyostelium* cells, we chose to use Latrunculin B (LatB), which is an inhibitor for actin polymerization [84], to impede cell motion. In this experiment, cells were harvested and mixed with 10-25 μM LatB in KN_2/Ca buffer before plating onto the TFM silicone substrate. This dosage of LatB completely halted actin polymerization, and as a result the cells did not show any motion and rounded up. GFP images and the kymographs of three aggregates are shown in Fig. 3.4a. By examining the dark bands in the kymographs, it was clear that the cAMP waves propagated as target waves (radially outward) as opposed to the rotational mode shown in Fig. 3.1a. Though, we also noticed two other effects of LatB that might have affected the signaling pattern. First, the geometry of the aggregate was no longer perfeclty round but rather irregular in shape. Second, the firing frequency of cAMP seemed to have been reduced ($T' \approx$ 10-20 mins), hinting that LatB might have altered the cAMP signaling dynamic at the cellular level. To further investigate these two effects, we decided to run more experiments.

First, instead of adding LatB before loading the cells onto the silicone substrate, we added LatB to the syringe connected to the microfluidic device right before starting the experiment. As it took time ($\sim$ 20 mins) for LatB to flow through the tubing to reach the device, cells were able to move around and rotate normally for a while, so that most aggregates became relatively circular in shape. Fig. 3.4b shows the snapshots of an aggregate right before and after exposure to LatB. In the GFP kymograph, the aggregate showed rotational motion and a rotating cAMP wave could be seen up to the moment that LatB reached the aggregate. After the exposure to LatB, the cAMP signaling was initially not observable but then resumed in the form of target waves. In this experiment, a total of 6 aggregates was monitored and they all showed similar behavior. The averaged traction force and cell velocity for these aggregates were calculated (Fig. 3.4c).

Within 10 mins upon LatB treatment, the radial traction force quickly dropped from 400 Pa to 100 Pa, while the tangential force dropped from 15 Pa to less than 5 Pa. Meanwhile, both radial and tangential velocities went down to zero. As in the irregularly shaped aggregates shown in Fig. 3.4a, these round aggregates also show a qualitative change in signaling dynamics from spiral waves to target waves. Thus the aggregate shape did not appear to be responsible for the change in cAMP wave patterns.

Next, we sought to elucidate the effect of LatB on cAMP signaling dynamics, specifically whether it would alter the wave period or wave speed. We performed experiments in which starved cells were deposited to the bottom of a glass plate to form a dense confluent layer of cells. As the cells developed, cAMP waves that propagated through the cells were observed and analyzed (Fig. 3.5). We compared the results with and without the addition of LatB in a large field of view ($\sim 1900\ \mu m \times 1900\ \mu m$). Period of the waves was calculated using auto-correlation of the GFP intensity at several locations, after which the average was plotted as a function of time (Fig. 3.5c-d). For both with or without LatB, the periods decreased over time as similarly reported during the normal developmental program of *Dictyostelium* cells [66, 85]. Without LatB, the period decreased from about 20 mins to 10 mins in two and a half hours. With LatB, the period reduced from roughly 30 to 15 mins. The speed of the waves was computed by fitting straight lines to an array of kymographs with different angles at 3 × 3 locations [86]. The calculated wave speeds were verified with manually tracked data points (black cross). In both cases, with or without LatB, the wave speed changed from $\sim 130\ \mu m/min$ to ~ 50 - $80\ \mu m/min$ in two and a half hours. Note that without LatB, as cells began to form isolated aggregates, the tracking of waves became infeasible which resulted in the absence of a computed wave speed after two hours. In total, three sets of experiments were done and when we focused on the common time frames where signaling was regular (i.e. small standard deviation in detected periods), the signaling period without LatB was 10 ± 2 min, while with LatB was 16 ± 5 min. For wave speed, normal condition was $100 \pm 60\ \mu m/min$ while with LatB it was $100 \pm 50\ \mu m/min$. Overall, LatB

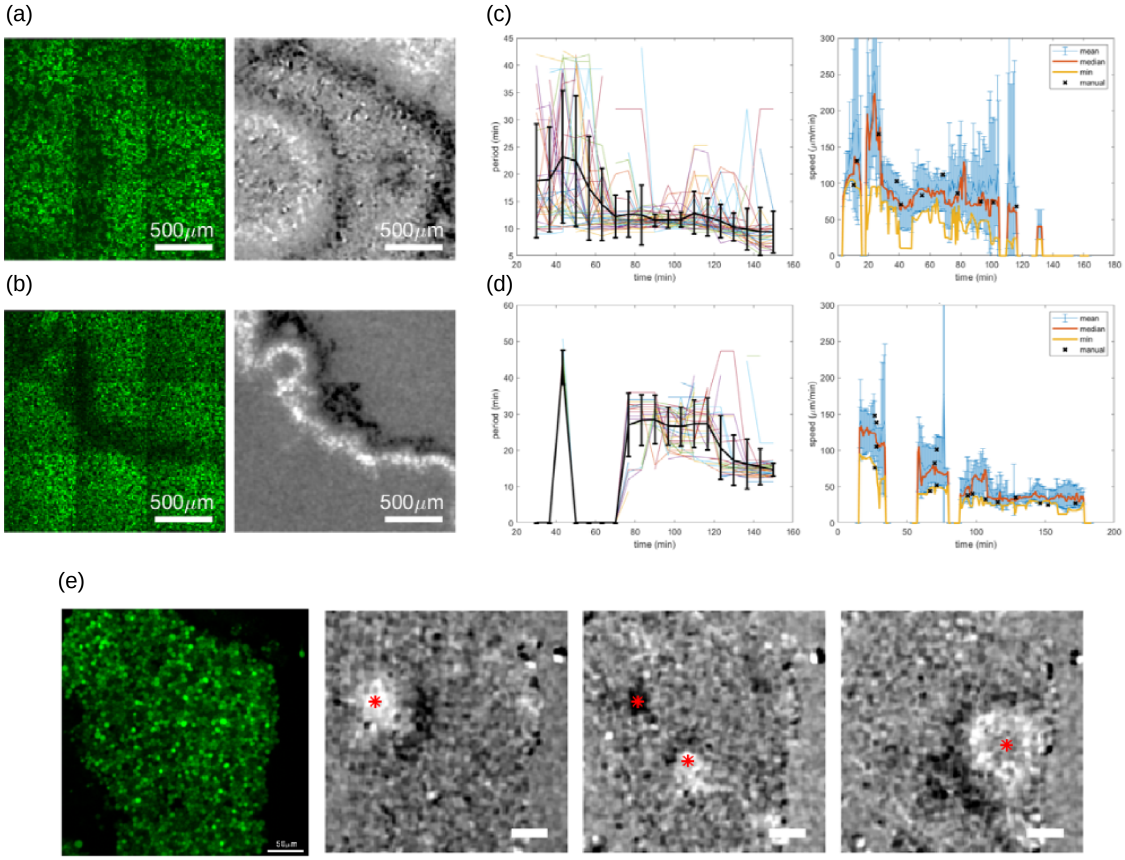

Figure 3.5: Determination of effect by LatB on wave speed and wave periods using confluent cell layers. In a large aggregate, which compensated the effect of increase in signaling period, only target waves could be observed. (a-b): [left] GFP images showing cAMP wave propagation in a confluent layer of cells, and [right] normalized difference images, $I = \frac{I_t - I_{t-1}}{(I_t + I_{t-1})/2}$, without (a) and with (b) LatB. (c-d): The period and speed of the cAMP wave as a function of time without (c) and with (d) LatB. (e): Example of a relatively large aggregate in the microfluidic device which displayed multiple target waves over time. Red asterisks marked the propagation center of a few target waves. Scale bar is 50 μm.

appeared to increase the signaling period by about 60 % while not affecting the wave speed. Our results are consistent with a previous study [87] where Latrunculin A increased the period of optical density waves oscillation in a dose-dependent manner.

Now, taken into consideration that LatB could increase the signaling period of *Dictyostelium* cells, we need to review how it might affect the spatial signaling pattern. Conveniently, according to Eq. 3.13, the number of spiral arms should be inversely proportionally to the refractory period τ, which in turn should be related to the signaling period. So, an increase in signaling period by LatB, should in fact decrease n and can result in values of n that are smaller than 1, so that no persistent rotating wave can be sustained. However, in the same equation, since $n \propto \frac{r^*}{\tau}$, the increase in signaling period can theoretically be canceled out with an increase in radius of the aggregate. In our experiment, the minimum radius to support a one-arm rotational wave was found to be $\sim 50\ \mu m$. Therefore, with LatB, with a 60 % increase in signaling period, we expect the minimum radius to increase to $\sim 80\ \mu m$. So, if cell motion was not important, we should expect to still observe spiral waves in LatB in large enough aggregates. For the LatB experiment described earlier (Fig. 3.4c), 2 out of the 6 aggregates were larger than 80 μm and only target waves were observed. In our experiments, even though we have many aggregates with a size larger than this minimum radius, we never observed spiral wave activity. As an example, Fig. 3.4e shows a large aggregate treated with LatB in the microfluidic device. Despite having a large radius ($> 130\ \mu m$), only target waves were observed. These results strongly suggest that cell motion is crucial for setting up persistent rotational cAMP wave within a cell aggregate.

3.6 Discussion

3.6.1 Origin of traction force in rotational mound

To understand the origin of traction force in the *Dictyostelium* rotational mound, we inspected various factors in our experiments. First, we noticed that there was a large radially outward traction force that the 2D mound exerted on the substrate. This outward boundary force existed not only in the solid mound, but also in other morphologies like the annuli and streams of cells. We verified that it was not due to the pushing effect of the ceiling of microfluidic device by looking at traction force of free 3D mounds, and confirmed that it was not related to the buffer flow in the device by running flow-free experiments. With the application of LatB, we prevented actin polymerization of the cells and the traction force of static aggregates were greatly reduced, though non-zero, compared to the rotational state. Finally, we conducted an experiment treating aggregates with phosphodiesterase (PDE), which decomposes cAMP, and measured that the traction force vanished to near zero (see appendix B.3). Our results suggest that actin polymerization in the cells and the presence of an external cAMP field are essential for traction force generation.

3.6.2 Motion-driven wave pattern formation

A few commonly known mechanisms for spiral wave initiation in excitable media is by the break up of the wavefront of a wave, by two waves initiating spatiotemporally close to each other within a vulnerable window or having spatial inhomogeneities in the medium [88]. Here, in our model, we show computationally a new motion-driven mechanism to initiate rotating spirals wave in a 2D aggregate of cells. In this mechanism, the collective cell motion is crucial in two parts. First, when cells rotate coherently, a singularity, which is a topological defect with charge +1, is created due to the collective alignment of cells. This singularity provides a basis for the cAMP spiral wave to propagate around, which also consists of a singularity at its core (the spiral tip). Together with the fact that cAMP wave can guide *Dictyostelium* cells movement, it forms a positive feedback between cell motion and cAMP signaling so that a persistent rotating spiral can be formed. Second, the magnitude of cell velocity modifies the propagation speed of the cAMP wave. This can be thought of as a Doppler effect. Since the cAMP-emitting cell is always moving in opposite direction to the propagating direction of the cAMP wave, the effective speed of the cAMP wave is lowered. This reduction in cAMP propagation speed increases the chance of a rotating wave to be formed, as shown in Eq. 3.13. From our simulation, this motion-driven mechanism provides a reliable way for the cells to initiate a stable rotational wave at a relatively low firing frequency. Finally, we verified experimentally that cell motion was essential for the existence of spiral waves in vertically constrained *Dictyostelium* cell aggregates, and that without cell motion, only target waves were observed.

3.7 Summary

In this study, we investigated the *Dictyostelium* mound stage by using novel methods to monitor cell movement (V), signaling activity (cAMP) and the traction force (T) exerted by two-dimensional aggregates. We found that these quantities are tightly correlated in the rotational state of the aggregates, showing oscillations of the same period. We presented the first measurements of traction force in the rotating 2D mounds revealing its spatial distribution and investigated the origin of the observed traction force pattern. More importantly, with our perturbation experiments and computational model, we studied the cAMP wave patterns in the 2D mounds and discovered that cell motion is crucial in initiating and sustaining the persistent rotational cAMP waves.

3.8 Acknowledgements

We acknowledge support from by the National Science Foundation under grant PHY 1707637 (W.-J. R.).

We thank Albert Bae, Elisabeth Ghabache and Richa Karmakar for sharing lab protocols and assistance in application of microfluidic device, traction force microscopy and transformation of the cell strain. The dissertation author was the primary author of this work.

Chapter 4

Matrix Degradation Determines Morphologies and Migration Modes of Cancer Cells in Dense Extracellular Matrix

4.1 Abstract

During tissue morphogenesis, different modes of collective migration of epithelial cells enable the formation of distinct multicellular structures, including ducts and acini. Understanding the rules determining these modes could inform regenerative medicine and cancer treatment. By studying the proliferation and development of cancer cells in dense extracellular matrix (ECM), we observed the formation of distinct structures and migration modes, namely rotating spheroids and invasive networks. Using experiments and mathematical modeling, we found that the spatial distribution of the matrix-degrading enzymes is a key factor in determining the morphologies and migration modes of the cancer cells.

4.2 Introduction

In the diagnosis of cancer, pathologists and physicians often evaluate the aggressiveness of the cancer by examining the morphological features of the tumor and its surrounding tissue. These morphological features have been used in some prognostic models and a strong association with the patient survival rates was found using clinical data [89]. Meanwhile, with the advance in next-generation sequencing technology, the amount of information on tumor genetics has been rapidly increasing. Using the Cancer-Genome-Atlas data, tumor morphology has been found to associate with the molecular content in cancer cells [90]. With this association, studying the tumor morphological patterns has the potential to guide patient selection in clinical trials and allow more precise patient care.

Cancer metastasis begins when the cancer cells migrate through the stroma into the blood or lymph vessels. During its migration, cancer cells exhibit a wide range of invasion strategies, from round or elongated single cells, to groups of cells migrating collectively. The migration modes can be influenced by a combination of stromal network structure, tumor cell signaling and extracellular stimuli [4]. This plasticity of cancer cells to adapt to the environment and switch between migration modes poses a great challenge to antimetastasis therapy. It has been suggested that future therapeutic efforts should focus on drugs that can selectively affect the actomyosin dynamics in cancer cell to prevent cancer invasion [91].

Here, we use experiments and mathematical modeling to gain understanding about the morphologies and migration modes of cancer cells by studying proliferating cancer cells in a controlled environment.

4.3 Experimental Results

Detailed experimental materials and methods can be found in Appendix C.

When single cells of breast cancer cells, liver cancer cells and human mammary epithelial

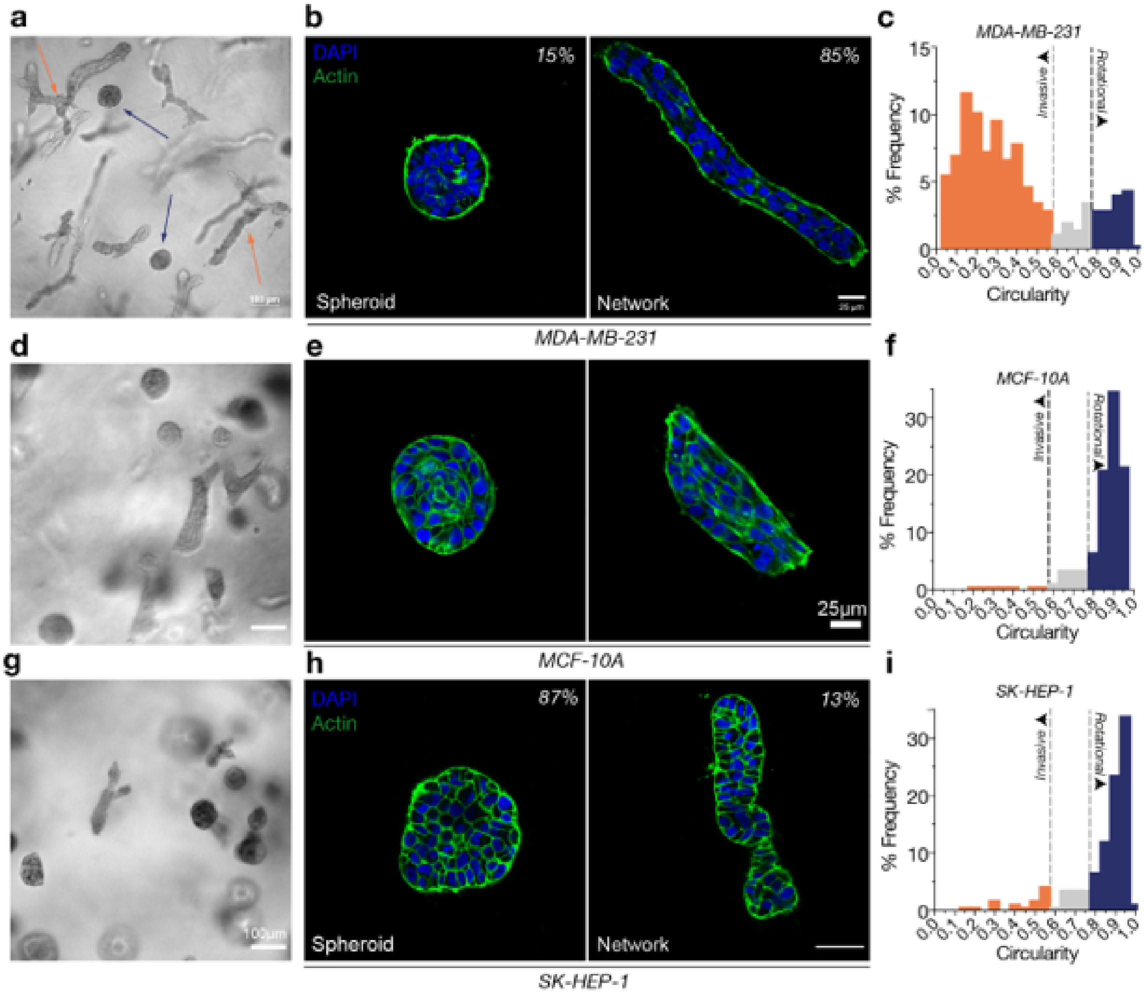

Figure 4.1: Organoids of cancer cells and epithelial cells form spheroids and networks in high density collagen. (a-c): Plots for MDA-MB-231 breast cancer cells. (a): Cancer cells seeded as single cells in high density collagen and cultured for 7 days. (b) Immunofluorescence images of networks vs spheroids showing the nucleus (DAPI) and actin of the multicellular structures. (c): Plot of percentage of each phenotype: invasive network and rotational spheroid. (d-f): Plots for MCF-10A human mammary epithelial cells. (g-i): Plots for SK-HEP-1 liver cancer cells.

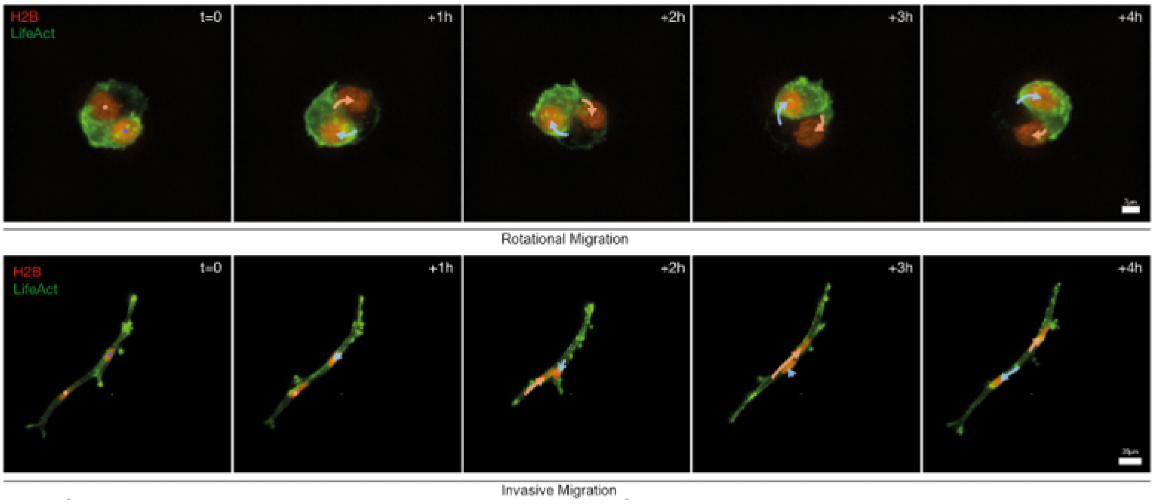

Figure 4.2: Two migrations modes are associated with the two morphologies observed in MDA-MB-231 breast cancer cell organoids. Upper row: rotational cells associated with spheroids. Lower row: invasive cells associated with networks.

cells were seeded and cultured for 7 days in dense ECM, multicellular structures with two distinct morphologies were observed (Fig. 4.1a,d,g). By considering the circularity of the multicellular structures, spheroids and networks were identified and the plot of the percentage of each phenotype are shown in (Fig. 4.1c,f,i). These two structures were observed across all three cell types (Fig. 4.1b,e,h).

When we examined the cell cultures at an early stage (1-2 days) during which 2-cell clusters were formed, we observed that the two distinct morphologies were associated with two distinct migration modes — rotational and invasive as shown in Fig. 4.2. The rotational cluster was characterized by its rounded shape while the two cells were rotating around the center of the cluster. The invasive cluster consisted of elongated cells with the two cells showing linear motion along their elongation axes, occasionally sliding past each other. These rotational and invasive clusters were found to develop into spheroids and networks respectively at later time points.

More data quantification between the rotational and invasive clusters can be found in Appendix. C.3.

4.4 Model Results

4.4.1 Model Setup

To explore the plausible mechanisms leading to the two distinct morphologies and migration modes observed in the cancer cell organoids, we developed a Cellular Potts Model (CPM) with cell motility, cell-ECM interactions and proliferation. The basic setup of the model has been outlined in Sec. 3.4. Here, we focus on the additional modules specific to modeling cancer cells in dense ECM.

Cell motility

Cell motility of the cancer cell is modeled using the same polarization module as presented in Sec. 3.4. The motivation is that cancer cells and amoeba cells both show similar plasticity in their two main migration modes — mesenchymal mode and amoeboid mode. The crawling motion of the cells involves positive feedback between motion and actin polymerization, which is captured by the polarization vector shown in Eq. 3.4, 3.6 and 3.7.

Cell-ECM interactions

For cell-ECM interactions, we consider two contributing factors — cell-ECM adhesion and ECM degradation.

Cell-ECM adhesion is modeled similarly compared to the cell-cell and cell-media interactions described in Sec. 3.4. The strength of the cell-cell ($J_{c,c}$) is slightly lower than strength of the cell-ECM ($J_{c,e}$). This ensures that cells are moving collectively as observed in experiments. Although this not the focus of our study, we have also included the possibility of cell-media interaction ($J_{c,m}$). This interaction was chosen to be higher than both $J_{c,c}$ and $J_{c,e}$, such that the cells would try to minimize the cell-media surface.

For ECM degradation, we consider a diffusible matrix-degrading enzyme (E) produced by the cells. It has been shown that cancer cells can release proteases, mainly Matrix Metalloproteinases (MMPs), that degrade the fibrous extracellular matrix [92]. In our model, there are two modes of degradation employed by the cells — local and global degradation. In the mode of local degradation, each individual cell only releases the enzymes locally at the tip of the cell, determined by the direction of the polarization vector (P). This is implemented by a rule-based fashion where the dot product between the position of each element in the cell ($r_{i,j}$) and the polarization vector (P) is calculated. Then, local production of the enzymes only takes place at elements that have magnitude of the dot product higher than the 99% of the maximum magnitude. In addition, the local production only occurs when the cell element is in contact with an ECM element (i.e. at least 1 out of 8 neighboring sites has to be an ECM site). For the global mode of degradation, the release of enzyme is non-directional and constant over the whole cell body. The dynamics coupling the matrix-degrading enzyme (E) and the ECM substrate (S) is described by the equations below:

$$\frac{dE}{dt} = D\nabla^2 E + k_g\delta(\sigma_{i,j} - \sigma_{cell}) + k_l\delta(\sigma_{i,j} - \sigma_{cell,tip}) - k_d E \; - \; k_r ES \tag{4.1}$$

$$\frac{dS}{dt} = -\, k_r ES \tag{4.2}$$

$$\sigma_{cell,tip} = P_{i,j} \geq 99\% \times \max_{\forall i,j}(\vec{r_{i,j}} \cdot \vec{P}) \tag{4.3}$$

In Eq. 4.1, the first term describes the diffusion of the enzyme with diffusion coefficient D; the second and third terms represent the global and local production of the enzyme where δ is the kronecker delta, k_g and k_l are the respective rates of production; the fourth term is the auto-degradation of the enzyme with degradation rate k_d and the fifth term is the reaction with ECM with reaction rate k_r.

Lastly, to model the physical barrier of ECM, an ECM penetration cost is included in the

Hamiltonian:

$$H_{ECM\,penetration} = \lambda_{ECM} \sum_{i,j \in \sigma_{cell}} S_{ij} \tag{4.4}$$

The penetration energy cost is proportional to the concentration of the ECM (S) and the parameter that indicates the strength of ECM (λ_{ECM}). When a cell element successfully overcomes an ECM element, the lattice site of the ECM will be updated to the invading cell label regardless of the original ECM value.

Proliferation

The proliferation of cells in our model involves two steps — growth and division. For growth, we assume that the target size of the cell is a function of time, $A(t)$. In each simulation step, the target size of individual is increased by the growth rate $G(t)$ such that

$$\begin{aligned} \frac{dA(t)}{dt} &= +G(t) \quad (4.5) \\ G(t) &= \frac{G_0}{k^t} \quad (4.6) \end{aligned}$$

Eq. 4.6 models the reduced growth rate over time (k > 1) that accounts for the difference in 2D proliferation in our simulation, compared to 3D proliferation observed in experiment. If we consider the number of cells in a spherical cancer organoid, in the 2D case $N_{2D} \sim R^2$ while in 3D $N_{3D} \sim R^3$ where R is the radius of the organoid. Thus, the number of cells in 2D (cross-sectional) actually corresponds to a larger number of cells in 3D, with correction factor $N'_{2D \to 3D} = N_{2D}^{3/2}$. Therefore, a constant growth rate in 3D (experiment) would correspond to a reduced growth rate over time in 2D (simulation). Since the exact correction factor depends on the morphology of the organoid (not necessarily spherical), the value of k was decided empirically to match the numbers of simulated cells to the numbers of cells observed in experiments on the 2nd day and 7th day following cell seeding. Lastly, we impose a maximum cell size A_{max} such that the cell will not grow indefinitely.

For division, we employ a stochastic approach such that when the cell area exceeds a threshold value ($A_{thres} = pA_{max}$, with p equals 0.85 in our model), it will divide into two smaller cells with a fixed probability at each simulation step. The division takes place at the middle of the long axis of the dividing cell, such that the two daughter cells will have half the size of the mother cell. One of the daughter cell will maintain the cell label of its mother while a new label will be created for the other daughter cell. Finally, the daughter cells will inherit the velocity and polarization vector of their mother cell.

4.4.2 Two plausible mechanisms suggested by simulations

Using our model, we identified two plausible mechanisms which can lead to the distinct morphologies and migration modes of the cancer cell organoids that were observed experimentally.

Polarization persistence

We define the polarization persistence as $\gamma = \frac{k_+}{k_-}$ according to the polarization vector (Eq. 3.6 and 3.7). Since k_+ is the rate of production and k_- is the rate of degradation of the polarization vector, the ratio between the two rates determines how fast the polarization vector is updated, thus relates to its persistence. When we vary γ, we observe a strong effect on the morphologies and migration modes of the organoids (Fig. 4.3). At low γ (Fig. 4.3a), when degradation dominates, the polarization vector is short-lived such that the cells change direction more quickly, resulting in a rotational morphology that is already established at the two-cell stage. At high γ (Fig. 4.3c), the polarization degrades slowly such that the polarization vector is more persistent, resulting in linear motion of the cells forming the invasive network structure. At intermediate γ (Fig. 4.3b), a transient form is observed where it is a multicellular structure characterized by the presence of a few sprouting tips, representing a hybrid between the rotational spheroids and invasive networks.

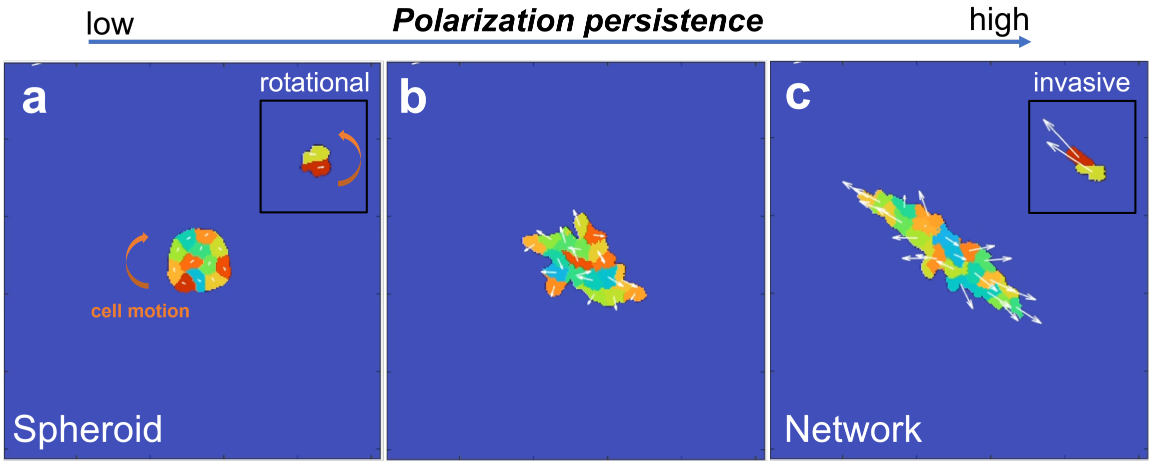

Figure 4.3: Model results showing morphologies of cancer cells depended on polarization persistence. (a-c): Morphology of simulated cancer cell organoid on day 7 as function of polarization persistence $\gamma = \frac{k_+}{k_-}$. Insets show the migration mode of the two-cell stage on day 1. (a) At low γ, a rotational spheroid is formed. (b) At intermediate γ, a transient structure with sprouting tips is formed. (c) At high γ, the cells move persistently and an invasive network structure is formed. White arrows indicate magnitude and direction of the polarization vectors.]

From these numerical results, we predict that ratio between the actin polymerization (k_+) and depolymerization rate (k_-) is a key factor determining the formation of rotational spheroids and invasive networks.

Modes of degradation

The second mechanism considers the modes of degradation. When we vary the production rates of the matrix-degrading enzyme, k_g and k_l for global and local degradation respectively, we again see a strong effect on the morphologies and migration modes as shown in Fig. 4.4. When global degradation dominates (Fig. 4.4a), the cells degrade the surrounding ECM evenly in all direction, resulting in the formation of rotating spheroids. When local degradation dominates (Fig. 4.4c), the cells release the enzymes at the tip determined by the polarization vector, such that the ECM is being degraded along the direction of cell motion which is roughly linear, resulting in the formation of an invasive network. While in the intermediate range 4.4b), when the global and local degradation are comparable, a transient structure with some sprouting tips is formed. Our

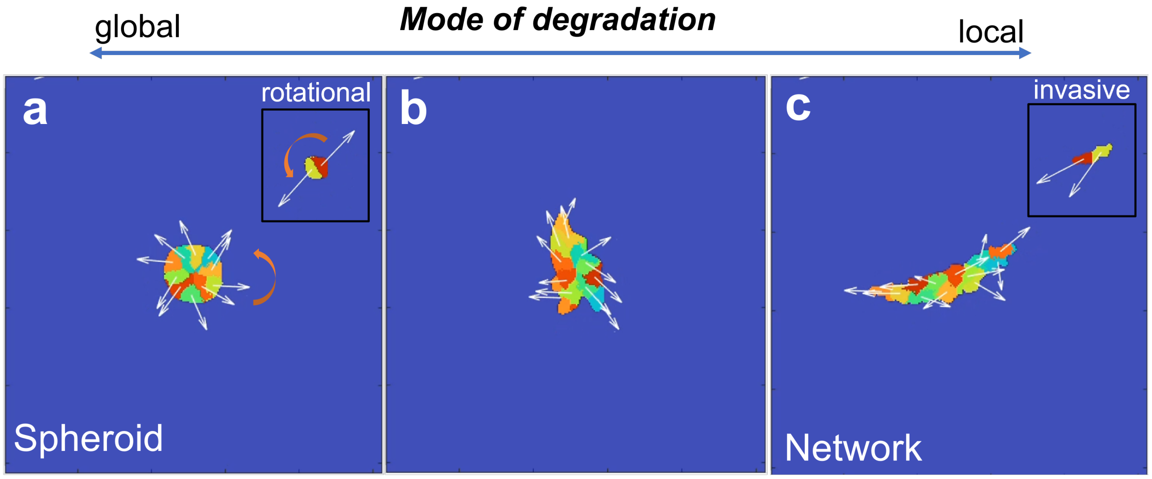

Figure 4.4: Model results showing morphologies and migration modes of cancer cells depended on mode of degradation. (a-c): Morphology of simulated cancer cell organoid on day 7 as function of modes of degradation determined by the rates of global and local production, k_g and k_l respectively. Insets show the migration mode at the two-cell stage on day 1. (a) When global degradation dominates, a rotational spheroid is formed. (b) When rates of global and local degradation are comparable, a transient structure with sprouting tips is formed. (c) When local degradation dominates, the cells move persistently and an invasive network is formed. White arrows indicate magnitude and direction of the polarization vectors.

results suggest that the localization of the release of matrix-degrading enzymes can lead to the formation of the distinct morphologies and migration modes observed in experiments.

4.5 Model Verification and Perturbation Experiments

Model prediction on modes of degradation

Changing the actin polymerization rate in experiments is challenging, since it will affect a large number of cellular processes. Therefore, we decided to focus on exploring how the modes of degradation might affect the morphologies and modes of migration. In Fig. 4.5, we show the phase space plot of circularity of the 2-cell structure as a function of global and local production rates (k_g and k_l) of the matrix-degrading enzyme. In this plot, we have indicated the boundary between rotational and non-rotational structures by a red dotted line. In addition, the boundary

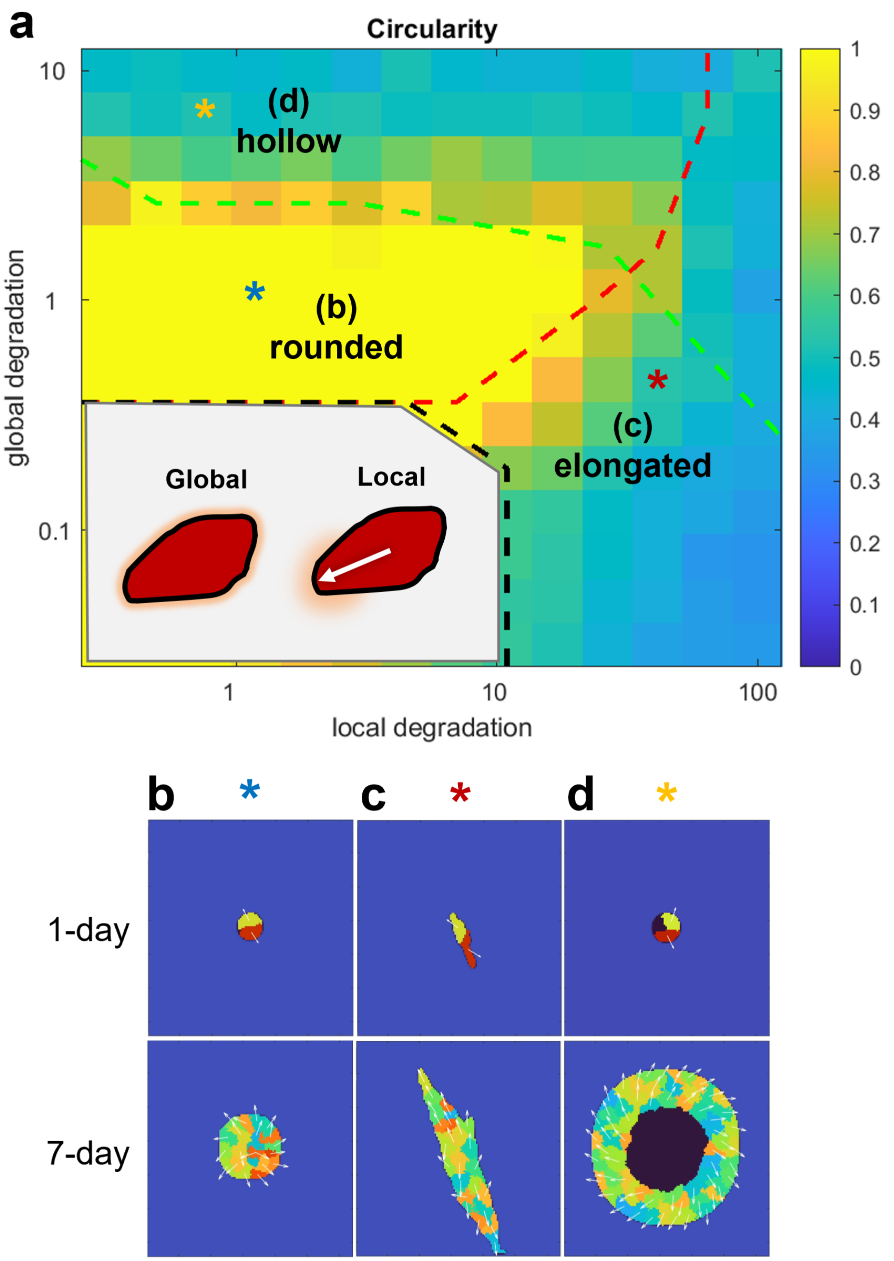

Figure 4.5: [Model phase space showing different morphologies of cancer cells as a function of modes of degradation. (a): Circularity of the simulated 2-cell stage of cancer cells on day 1, as a function of the global and local production rates of matrix-degrading enzyme. The colored asterisks indicate examples of a (b) rounded, (c) elongated and (d) hollow structure. The red dotted line separates regions with high rotational speed (left to line, $\geq 0.6 rad/h$) and low rotational speed (right to line, $< 0.6 rad/h$). The green dotted line separates regions with high cells to degraded ECM volume (below the line, $\frac{V_{cells}}{V_{ECM}} \geq 80\%$) and low cells to degraded ECM volume (above the line, $\frac{V_{cells}}{V_{ECM}} < 80\%$). (b-d): The morphologies and migration modes of the cells on day 1 and day 7 corresponding to the asterisks located in (a).

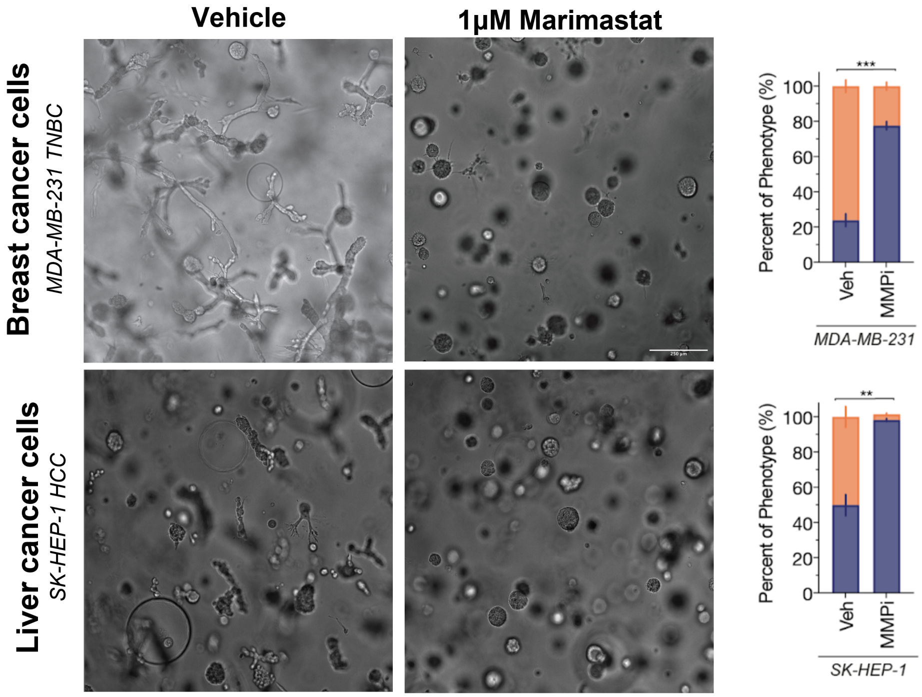

Figure 4.6: When the MMP inhibitor, $1\mu M$ Marimastat, is added to the extracellular matrix, local degradation is inhibited and a majority of spheroids is formed (right) compared to the vehicle (left) for both breast cancer cell (upper) and liver cancer cell (lower). Percentages of each phenotype (blue: spheroid, pink: network) is shown in the rightmost panel.

between solid and non-solid structures is shown as a green dotted line. Examples of a rotational spheroid, invasive network and hollow spheroid are shown in (b), (c) and (d), respectively, for both the 1-day and 7-day stage. As can be seen from the phase plot, we predict that inhibiting local degradation will results in the formation of rotating spheroids.

Perturbation Experiments using MMP inhibitors

To perturb the degradation modes employed by the cells, we applied $1\mu M$ Marimastat, a MMP inhibitor, to the extracellular matrix. In a previous study [93], it was shown that local degradation is related to MMP-14, which is a transmembrane protein capable to cleave type I collagen. Marimastat can inhibit the expression of MMP-14 [94] which can in turn inhibit local degradation of the cancer cells. In Fig. 4.6, we show that with $1\mu M$ Marimastat, the multicellular structures formed on the 7th day became mostly spheroids compared to the vehicle where substantial amount of invasive networks were observed. These results verified our model prediction that the mode of degradation is a key factor in determining the morphologies and migration modes of the cancer cell organoids.

4.6 Summary

In this study, we presented observations of two distinct morphologies and modes of migration — namely rotational spheroids and invasive networks, in the cancer cell organoids plated in dense extracellular matrix (ECM). These structures were observed across breast cancer cells (MDA-MB-231 TNBC), liver cancer cells (SK-HEP-1 HCC) and Human Mammary Epithelial Cells (HMEC), suggesting that cell-cell adhesion and laminin deposition do not determine formation of the distinct structures. Using mathematical modeling and perturbation experiments, we found that the mode of degradation is a key factor in determining the morphologies and migration modes of the organoids.

4.7 Acknowledgements

We acknowledge support from by the National Science Foundation under grant DMS-1953469 (W.-J.R.). The dissertation author was one of the primary authors of this work.

Appendix A

Methods and Materials for Chapter 2

A.1 Microfluidic device, device preparation, and experimental setup

The microfluidic system produces bell-shaped pulses of concentration that periodically sweep over cells on the substrate, thus emulating the spatial and temporal pattern of concentration in a periodic traveling wave. The microfluidic system is comprised of a microfluidic device and a flow-driving setup, which are modified versions of the device and setup described in our previous publication [21]. The microfluidic device consists of a micromachined polydimethylsiloxane (PDMS) chip and a #1.5 microscope cover glass substrate with a periodic micropattern of stripes of polyethylene glycol (PEG) gel. The PEG-gel stripes are all $\sim$1.5 μm high and $\sim$30 μm wide and one of two substrate patterns are used: 1) one 25 μm wide glass (non-treated) stripe for every four 10 μm wide glass stripes or 2) variable width stripes, repeated every 6 stripes, ranging from $\sim 6\mu$m to $\sim 25\mu$m (Fig. 2.1d-e). We have verified that our results are independent of the stripe width. Because developed *Dictyostelium* cells cannot adhere to the surface of PEG-gel, adherent *Dictyostelium* cells are confined to glass stripes, making their migration along the 10 μm wide glass stripes nearly one-dimensional (1D) [50].

The microfluidic device has three inlets (A-C) and one outlet (see Fig. 1). Its main functional area is an ∼100 μm deep chemotaxis channel with a width of 2200 μm and an ∼7 mm long rectilinear part. At the entrance of the chemotaxis channel, a ∼200 μm wide stream of a concentrated solution of cAMP (coming from inlet C) is squeezed (hydrodynamically focused) between two streams of plain buffer or of cAMP solutions with a lower concentration (coming from the inlets A and B), which together fill the rest of the 2200 μm wide chemotaxis channel. As the focused stream of cAMP advances down the chemotaxis channel (along the y-axis), the diffusion of cAMP molecules across the boundaries of the stream gradually changes the lateral (across the flow, x-axis) profile of cAMP from its initial rectangular shape to a bell-shaped curve. At the standard experimental conditions, [cAMP] in the concentrated solution is 1400 nM, the mean flow velocity in the gradient channel is ∼300 μm/s, and the chemotaxis is observed ∼3 mm downstream from the gradient channel entrance, where the maximal [cAMP] is reduced to ∼1000 nM, and the effective width of the stream of concentrated cAMP (full width at half height) is increased to ∼230 μm, both due to diffusion of cAMP across the stream [21]. The microfluidic system operates in a cyclic fashion. In the beginning of a cycle, the volumetric flow rate of the stream of buffer (or low-concentration cAMP solution) from inlet B to the right of the cAMP stream is low, and the volumetric rate of flow of buffer from inlet B to the left of the cAMP stream is high, thus placing the cAMP stream close to the right wall of the gradient channel. The flow rate of the buffer stream on the right linearly increases with time, while the flow rate of the buffer on the left linearly decreases with time, with the total flow rate remaining nearly unchanged. As a result, the high concentration cAMP stream (which is squeezed between the buffer streams) linearly drifts from right to left, and, at a given y-axis position, a bell-shaped pulse of cAMP is sweeping from right to left (in the negative x-axis direction) at a constant speed. The length of the sweep is l≈1425 μm that for a duration of the sweep T=10 min results in a speed of 2.5 μm/s for the motion of the cAMP pulse across the gradient channel (note that it takes 30s for the wave to be reset, such that the effective duration is 570s). At the end of a sweep, the flow of the concentrated cAMP solution is turned off, making the concentrated cAMP to completely disappear from the gradient channel, and then the flow rates from inlets A and B restored to their initial values. After that, the flow of the concentrated cAMP solution is turned on again, making the stream of concentrated cAMP reappear at its initial location close to the right wall of the gradient channel, and the next cycle begins. Importantly, the cAMP stream is effectively moved from its final to initial location without directing it (even transiently) anywhere else in the chemotaxis channel. Also, because of the relatively large length of the sweep, and fast decay of [cAMP] with the distance from the peak of the bell-shaped profile, there is $\sim$500 μm wide region near the middle of the gradient channel, where [cAMP] is very close to the background concentration, both in the beginning and end of each cycle. As a result, all cells in this region are exposed to the same periodically repeating spatiotemporal pattern of [cAMP] and can be pooled and analyzed together, after accounting for a time difference within a cycle of $\Delta t = \Delta x / v_x$, where Δx is the distance between cells along the x-axis. Therefore, large sets of data on chemotactic indices (CIs) and velocities of individual cells at different time points (phases) of the repeated cAMP wave cycle can be collected.

Further details on the operation of the microfluidic device and flow setup and on the experimental procedure as well as a detailed mathematical analysis are provided in SI of Ref. [21]. The following modifications were made to the original experimental setup and procedure of Ref. [21]. (1) Because flow in the microfluidic device is driven and controlled by applying differential pressures between the inlets and the outlets, it is necessary to have substantial fluidic resistances between the inlets and the outlet. In the original device, those resistances were implemented in 100 μm deep and 60 μm wide channels, making the device easy to fabricate (all channels had the same depth), but requiring the resistance channel lines to be long, because of their relatively low fluidic resistance per unit length. In the present device, the resistance lines are $\sim$30 μm deep and $\sim$30 μm wide channels, which have an $\sim$40 larger fluidic resistance per unit length, greatly reducing the footprint of the microchannel network (at the expense of making the fabrication of the device somewhat more involved). (2) The reduced footprint of the microchannel network makes it possible to seal the PDMS chip against the coverglass with the micropattern of PEG-gel stripes using the application of vacuum ($\sim$ -30 kPa) to a deep (100 μm) and wide (4 - 6.5 mm) O-shaped grove around the microchannel network that acts as a vacuum cup. This vacuum-assisted sealing is essential, because it allows keeping the micropatterned substrate wet at all times, thus preserving the structure and functionality of the PEG-gel stripes (that *Dictyostelium* cells cannot adhere to). (3) The possibility of attaching the microfluidic chip to a wet substrate also enables direct plating of *Dictyostelium* cells onto the substrate. The PDMS chip is attached to the substrate only after cells settle and adhere to glass stripes. As a result, cell plating is substantially simplified and streamlined as compared with the original microfluidic device, where cells needed to be delivered to the gradient channel through a dedicated inlet and connecting microchannel that are both absent in the present device.

Microfluidic chips were cast in polydimethylsiloxane (PDMS, Sylgard 184 by Dow corning) using a microfabricated master mold, a 5 inch silicon wafer with a micro-relief of UV-curable SU8 photoresist (by MicroChem) produced with UV photolithography [50]. First, an $\sim$30 μm thick layer of SU8 2015 photoresists was spin-coated onto the wafer, pre-backed, exposed to collimated UV-light through a photomask, and post-baked. Next, the wafer was spin-coated with SU8 2050 photoresist to a total thickness of 100 μm, pre-baked, exposed to UV-light through a second photomask, post-baked, and developed, revealing a micro-relief with 30 μm and 100 μm tall micro-ridges. The 30 μm deep micro-grooves on the PDMS replica of the mold produced the 30$\times$30 μm resistance channels, and 100 μm deep micro-grooves produced all other flow channels and the O-shaped vacuum cups. The PDMS cast was cut into individual chips, and the inlet and outlet holes in the chips were punched with a Luer stub.

To verify the wave profile computed from numerical simulations of the diffusion process [21], we added Alexa Fluor$^{\text{TM}}$ 594 Hydrazide (Invitrogen), a fluorescent dye, to the cAMP solution. The fluorescent intensity profile with cAMP_{bg}=0 was well fitted using a Gaussian

$$\text{cAMP}_{\text{Gauss}}(x) = Ae^{\frac{-(x-x_0)^2}{2\sigma^2}}$$

where the wave peak position was given by x_0, the wave width was given by σ and its amplitude by A. Using the numerical simulations, this amplitude was determined to be 1000 nM at the experimental field of view [21]. An example of a fit is given in Fig. 2.1b-c. From these fits, we determined σ = 115 μm, corresponding to a full width at half maximum of 230 μm. Furthermore, by using a linear fit to x_0 as a function of time, we verified that the wave speed is v = 2.5 μm/s. For non-zero cAMP_{bg} the cAMP concentration was the Gaussian profile plus a constant equal to the value of cAMP_{bg} such that the total cAMP profile is given by $\text{cAMP}(x) = \text{cAMP}_{\text{Gauss}}(x) + \text{cAMP}_{\text{bg}}$.

A.2 Cell tracking

A machine learning (ML) model was developed for reliably tracking the complex movement of the *Dictyostelium* cells. 20 videos of cells moving in response to chemical gradients were provided for training of the model. In order to avoid having too many repeated or similar images, only one in every thirty frames was used for training and validating the model, resulting in 140 images. Each of the images, of size 256x256 pixels representing 25% of the full field of view, was assumed to be completely independent. Images were converted to grayscale and normalized. The model used was a U-Net convolutional neural network, which can be trained on very few images and outperforms most existing methods [95]. The model consisted of three rounds of convolution and max pooling, followed by a fully connected layer with 512 elements, and finally three rounds of convolution and upsampling. The convolution layers were 3x3 with 32, 64, and 128 filters. Rectified linear unit (Relu) activation was applied after each convolution. The pooling and upsampling layers were 2x2. Data augmentation, including shifting and flipping of the images, was used during model training to increase the size of the dataset. A labeled dataset was obtained by marking the centroid of cells in a small number of images using human input. A U-Net model was then trained on this small sample and then used to aid in marking further images. This process was repeated several times until the entire dataset was marked. The labeled dataset was then split with 80% of all images used for training, and 20% used for validation set. In order to avoid target leakage, the model's parameters and hyperparameters were reset and trained only on the new training dataset. Data augmentation was again used to increase the size of the training dataset. The final model consistently tracked 90% of all cells in the validation dataset. Finally, the model was tested on a new set of videos not seen in the original dataset. A comparison between blinded, manual marking of cells and the ML algorithm showed that approximately 97% of cells were tracked by the automated procedure (5623 vs. 5487).

Once cell positions were determined, we computed cell trajectories by connecting nearest points in consecutive frames. Only cells that were within a 300 μm wide region at the middle of the gradient channel were considered. These cells experienced a full cAMP wave, starting and ending at the background concentration. Furthermore, we only included cells that were continuously recognized for more than 3.5 min, that were moving with an average speed of at least 0.16 μm/min, and that were at least 33 μm from the neighboring cells (these cells are marked by red circles in Fig. 1). In addition, although rarely observed, cells moving on the PEG-gel stripes were also excluded. Data from the first cAMP wave was excluded to eliminate any initial differences in cells.

The cell's velocity in the x-direction for a given frame, V_x, was computed as the difference in the x-position 3 frames prior and 3 frames after the given frame, divided by the time interval between these frames (90s). The time with respect to the passage of the cAMP peak (phase) was assigned by measuring the distance of the cell from the location of the peak of the wave relative to the extent of the sweep. The CI as a function of time was computed by averaging data points in equally spaced bins of width 0.5 min. The time averaged CI, $\langle \mathrm{CI} \rangle$, was computed by averaging

CI in time over the entire wave cycle. The time average of V_x, $\langle V_x \rangle$, was calculated in a similar fashion. Experiments were repeated at least three times for each cAMP$_{\mathrm{bg}}$. For each cAMP$_{\mathrm{bg}}$, a distribution (N = 10,000 trials) of sample mean was generated by bootstrapping over the replicate experiments, and the experimental averages and error bars reported in this study were the mean and standard deviation of this resampled distribution.

A.3 Parameter fitting

As mentioned in the main text, we minimize the loss function $L = \sum_{n=1}^{N} |x_{exp} - x_{sim}|/(N\sigma_{exp})$ to find the optimal parameters. This loss function compares N=54 experimental data points to simulation data (see main text). We take 46 discrete points from previous experimental data (detailed in Ref. [21]) and 8 points derived from the current study. As in Ref. [21], σ_{exp} was taken as the standard deviation of the experimental data or 50% of x_{exp} where standard deviations were not available.

Following Ref. [21], the 46 data points using previous studies were chosen as follows: 24 data points were taken from uniform dose response data where cells were exposed to uniform stimulus switching from 0nM or 100nM to higher concentrations [53]. The peak amplitudes, peak times and the state of memory module M were fitted (see also Fig. 2.4a-b). Additionally, 15 data points were chosen from gradient-to-uniform data obtained from experiments in which cells were first exposed to a gradient (0-100 nM across a 70 μm wide channel), followed by a uniform concentration of 0, 1, 10, 20 or 50nM [21]. These experiments, detailed in Ref. [21], quantified the localization of activated Ras, a directional sensing marker, using the Ras-binding domain of Raf tagged to GFP (RBD-GFP). The times for disappearance and reappearance as well as the ratios of fluorescence intensity before and after the switching from gradient to uniform concentration were fitted. As indicated from the experiments, we required the memory M_f to stay high (i.e., M_f=1) for a uniform concentration of 10, 20 and 50nM and to become low (M_f=0) for

0nM . The final 7 data points were chosen from gradient reversal data where the initial gradient was switched to a reversed gradient of 100-0nM, 75-25nM or 60-40nM across the gradient chamber. The ratios of fluorescent RBD-GFP intensity before and after the switching were fitted. The memory was required to reverse in the 100 to 0nM profile and remain unchanged in the 60 to 40nM profile. Further details of these data points can be found in Ref. [21].

The "new" 10 data points were chosen from the current background experiments with cAMP_{bg}= 0, 0.01, 0.5, 60 and 150nM. To match with the experimental results, which showed that cells have a high CI during the front of the wave for cAMP_{bg}= 0 and 0.01 nM, persistent high CI for cAMP_{bg}=0.5 and 60 nM, and significantly reduced CI for cAMP_{bg}=150nM, we required the front memory, M_f, at 2.5 minutes before the peak of the wave, when cells experienced a positive gradient, to be high for cAMP_{bg}=0, 0.01, 0.5 and 60nM and low for 150nM. At 5 minutes after the peak, at a near-zero cAMP concentration, M_f was required to be low for cAMP_{bg}=0, 0.01 and 150nM and high for cAMP_{bg}=0.5 and 60nM.

We fitted the five parameters (a, b, k_{Mem}, k_{S2} and Km_3) related to the memory module using the lower bound constraints of [0.001, 0.001, 0.005, 20, 0.0001] and upper bound constraints of [1, 1, 5, 200000, 1] in units of [nM, nM, $\text{nM}^{-2}\text{s}^{-1}$, s^{-1}, nM]. To minimize L we used simulated annealing, which avoids trapping in local minima of the parameter space, and uses an artificial temperature that is decreased during the parameter search such that sampling becomes more and more selective. In each iteration, a new parameter set was generated from the previous one with a step size based on this artificial temperature. The difference in the value of the loss function between the new and previous iteration was then computed. For a negative difference the new parameter set was automatically accepted while for a positive difference the new parameter set was accepted with a chance that ranged between 0 to 50% and which was based on the loss function difference and the artificial temperature. The search was carried out in log space to cover the wide range of parameter values and the algorithm was concluded when the difference in loss function became smaller than 0.01 for more than 500 iterations. Multiple runs of simulated annealing were conducted with randomized initial parameter values. At the end of each run, pattern search was applied to obtain more precise local minima, using Matlab routine patternsearch. In each iteration, this algorithm attempts parameters values at a fixed step from the previous parameters. If the loss function was reduced, the step size would be doubled in order to explore a wider space. If the loss function did not reduce, the step size would be halved. The parameter search terminated when both the change in loss function became smaller than 0.01 and the absolute step size became smaller than 0.0001 in log10 space.

The final parameters are listed in Table 1 and correspond to $L = 0.556$. As in Ref. [21] (Fig. S5b in that study), we can compare the simulation results with experimental results of Takeda *et al.*, which recorded the intensity of RBD-GFP following a sudden change in uniform cAMP concentration [53]. In Fig. 2.4a-b, we plot the numerically computed intensity peak, I_{peak}, and the time corresponding to the maximum peak amplitude, T_{peak} as lines. These results are in good agreement with the experimental results, plotted as symbols. When we consider the loss function L' that includes only the 46 data points from the previous experiments, the current parameter set gives $L' = 0.655$ while the original parameter set results in $L' = 0.731$.

Table A.1: Model parameters.

Parameter	Value	Parameter	Value
k_R	$0.002463\ nM^{-1} \cdot s^{-1}$	k_{-R}	$1.006\ s^{-1}$
k_E	$0.159\ s^{-1}$	k_{-E}	$0.159\ s^{-1}$
k_I	$0.139\ s^{-1}$	k_{-I}	$0.139\ s^{-1}$
k_{basal}	$0.000015\ nM$	k_{Mem}	$0.2550\ nM^{-2} \cdot s^{-1}$
a	$0.0239\ nM$	b	$0.3550\ nM$
k_S	$2000\ s^{-1}$	K_{m1}	$0.018\ nM$
k_{-S}	$2048\ s^{-1}$	K_{m2}	$0.001\ nM$
k_{S2}	$149.4\ s^{-1}$	K_{m3}	$0.0366\ nM$
M_f^{tot}	1	M_b^{tot}	1
R_f^{tot}	1	R_b^{tot}	1
S_f^{tot}	1	S_b^{tot}	1

Appendix B

Methods and Materials for Chapter 3

B.1 Kymograph analysis

The angle and distance kymographs showed in Fig. 3.1f, 3.4a-b were created by spatially averaging over bins of angle ($\Delta\theta = 7.5^\circ$) and distance ($\Delta\rho = 3.33\mu m$) of the GFP images. A 2D Gaussian filter (1 temporal + 1 spatial) was applied to reduce spatiotemporal noise. To find the rotational cAMP wave angular speed, straight lines were fitted to the dark bands of the angle kymograph (I). To do so, a 2D sliding median filter with large windows (using MATLAB colfilt function) was applied to find a background kymograph (I_{back}) as shown in Fig. B.1. We obtained thr normalized signal by subtracting the background from and the original signal ($I_{norm} = I - I_{back}$). The kymograph was binarized (I_{bin}) by checking whether the signal was local minima (using MATLAB islocalmin function). Straight lines in the kymographs were then detected using Hough transform (using MATLAB hough function). By calculating the average slope of the fitted lines, the angular velocity and thus the period of the wave can be determined.

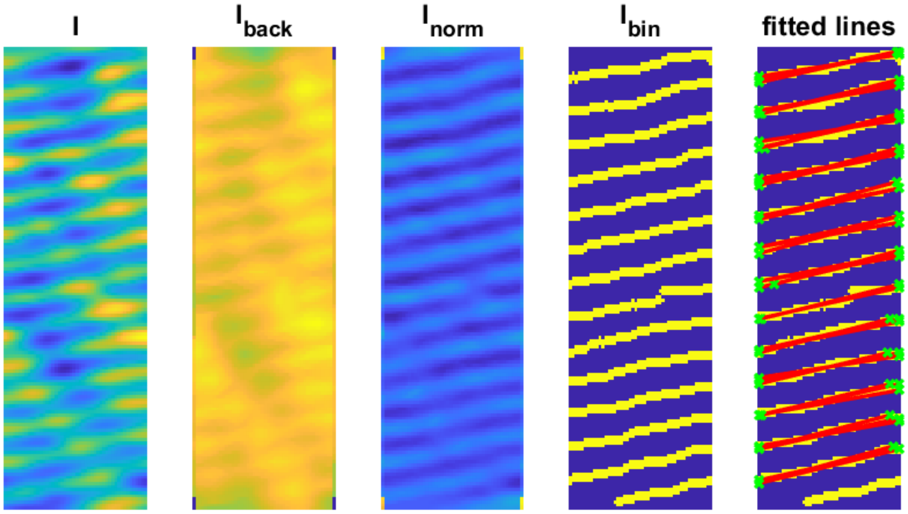

Figure B.1: Kymograph processing procedure in order to fit straight lines (red lines) to the dark bands in the kymograph by using Hough transform.

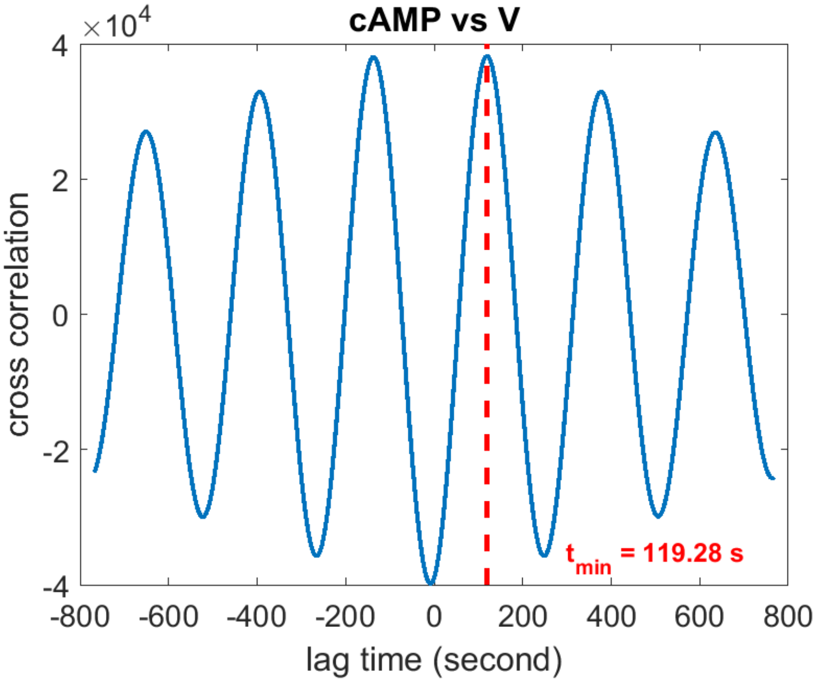

Figure B.2: The average cross correlation curve of cAMP and cell velocity of an aggregate. Time difference between the signals was found to be ~ 119.28 s as indicated.

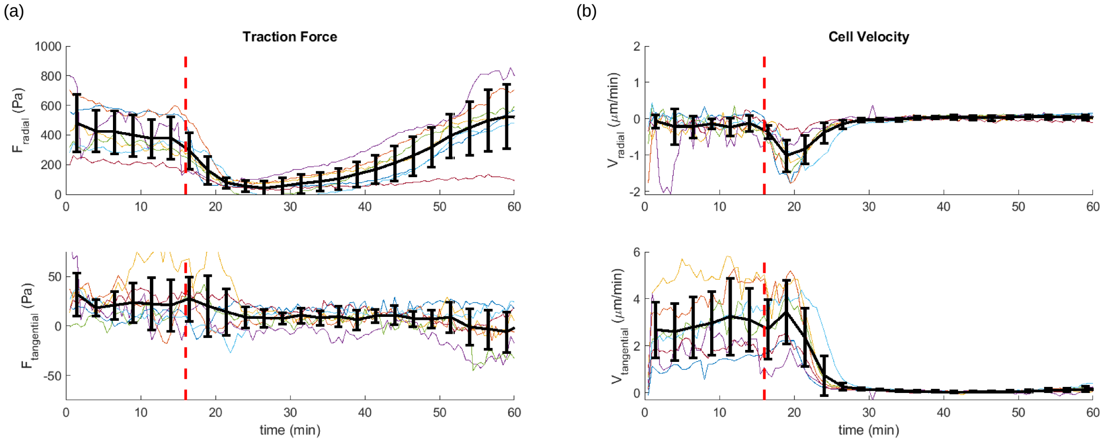

Figure B.3: Time series of (a) traction force and (b) cell velocity averaged over 7 aggregates in an experiment with the use of PDE. Upon the arrival of PDE, both traction force and cell velocity dropped to near zero. Red dotted line indicates the time when PDE reached the aggregates.

B.2 Phase difference calculation

To determine the phase difference between the pair of quantities as shown in Fig. 3.2b, we used cross correlation (MATLAB xcorr function). Specifically, for each pixel within the aggregate, cross correlation of the time series data (e.g. 'cAMP' and 'velocity') was calculated. Then we found the average cross correlation curve (Fig. B.2) by averaging over each pixel. The peaks (maximas) of the correlation curve were then identified and the one with the smallest absolute lag time was determined as the time difference Δt. Finally, we converted the time difference into phase difference by $\Delta\phi = 2\pi\frac{\Delta t}{T}$ where T is the average period of the signals.

B.3 PDE treatment on aggregates

$53\ \mu g/mL$ phosphodiesterase (PDE) in KN_2/Ca buffer was added in the syringe connected to microfludic, in similar fashion as the LatB experiments. Traction force and cell velocity time series are shown in Fig. B.3. Note that both traction force and cell velocity decreased to near zero upon the arrival of PDE. In the experiment, we observed that the initially rotating aggregate shrunk in radius while the rotation slowed down (see transient negative radial velocity). Meanwhile, cAMP signaling stopped. Later on, the cells seemed to be able to adapt to the increase in external PDE levels, and signaling resumed together with a gradual increase in traction force. Since PDE decomposes the cAMP, our results suggest that traction force generation attributed not only to actin polymerization and cell motion (as shown in LatB experiments) but also an external field of cAMP.

Table B.1: Model parameters.

Parameter	Value	Parameter	Value
$J_{c,c}$	50	ρ	0.5161 nMs^{-1}
$J_{c,m}$	700	g_c	0.0465 nM
λ_a	50	A	0.000574 nMs^{-1}
A	78 μm^2	K	0.00001 nM
λ_p	50	k_g	0.0970 $nM^{-2}s^{-1}$
λ_c	0.4	a	0.1863 nM
k_+	0.0129 s^{-1}	k_r	0.0839 s^{-1}
k_-	0.00645 s^{-1}	τ	93 s
D	0.129 $\mu m^2 s^{-1}$	Δx	1.25 μm
α_0	0.0516 nMs^{-1}	Δt	1.55 s
J	0.0645 s^{-1}		

Appendix C

Methods and Materials for Chapter 4

C.1 Cell culture

MDA-MB-231 breast cancer cells were ordered from ATCC (Manassas, VA) and SKHEP-1 were provided by Jason Sicklick (UCSD). All MDA-MB-231 and SK-HEP-1 cell lines were cultured in high glucose Dulbecco's modified Eagle's medium supplemented with 10% (v/v) fetal bovine serum (FBS, Corning, Corning, NY) and 0.1% gentamicin (Gibco Thermofisher, Waltham, MA), and maintained at 37 °C and 5% CO2 in a humidified environment. Cell lines were routinely tested for mycoplasma contamination (ATCC, Manassas, VA). To generate cells that express H2B-mCherry (pHIV-H2BmRFP, Addgene #18982 , Watertown, MA), LifeAct-GFP (Dendra2-Lifeact-7, Addgene #54694, Watertown, MA) and mCherry-LifeAct (Addgene, Watertown, MA), we generated viral particles by transfecting plasmids into lentiX 293T cells (Clonetech, Mountain View, CA) along with the psPAX2 packaging vector (Addgene #12260) and the pMD2.G envelop vector (Addgene #12259). Viral particles were collected by removing culture medium 24 and 48 hours after transfection and filtering through a 0.45μm filter. Transduced cells were treated with hexamethane bromide and a titration of viral particles for 24 hours. Selection with puromycin was conducted for plasmids with selection markers.

C.2 3D culture in collagen I matrix

Cells suspended in culture medium were embedded in 3D Collagen I matrices by mixing with 10x reconstitution buffer (1:1 v/v) and high concentration, rat tail acid extracted type I collagen (Corning, NY) to a final Collagen I concentration of 6 mg/mL. The pH was adjusted of the mixture using 1 N sodium hydroxide and polymerized via incubation at 37 degrees for 30 minutes.

C.3 Biophysical Gel Culture, Imaging, and Quantitative Analysis

To investigate the key factors driving these distinct morphogenic outcomes, we conducted measurements (Fig. C.1a) characterizing the four primary processes underlying cell migration: matrix remodeling, cytoskeletal dynamics, cell-matrix adhesion and contractility. Fig. C.1b-i show the comparison of the measurements between the two phenotypes. We found that there were significant differences in degradation and cytoskeletal polymerization measurements (C.1c,e) between the rotational and invasive cells, while cell-matrix adhesion and contractility did not show significant differences.

C.3.1 Biophysical Gel 3D Culture

MDA-MB-231 mCherry-LifeAct cells were suspended in culture medium (with or without pharmacological inhibitors) were mixed 1:1 v/v with 1x reconstitution buffer to achieve a final concentration of 100k cells/mL. Next, blue carboxylated microspheres (1 um, Thermofisher Scientific, Waltham, MA) were added to the cell-buffer mixture at a final concentration of 1:50 (v/v) of the final gel volume (200 μL). Dye-quenched (DQ) collagen type I (Thermofisher Sicentific, Waltham, MA) was added to the cell-buffer solution at a final working concentration

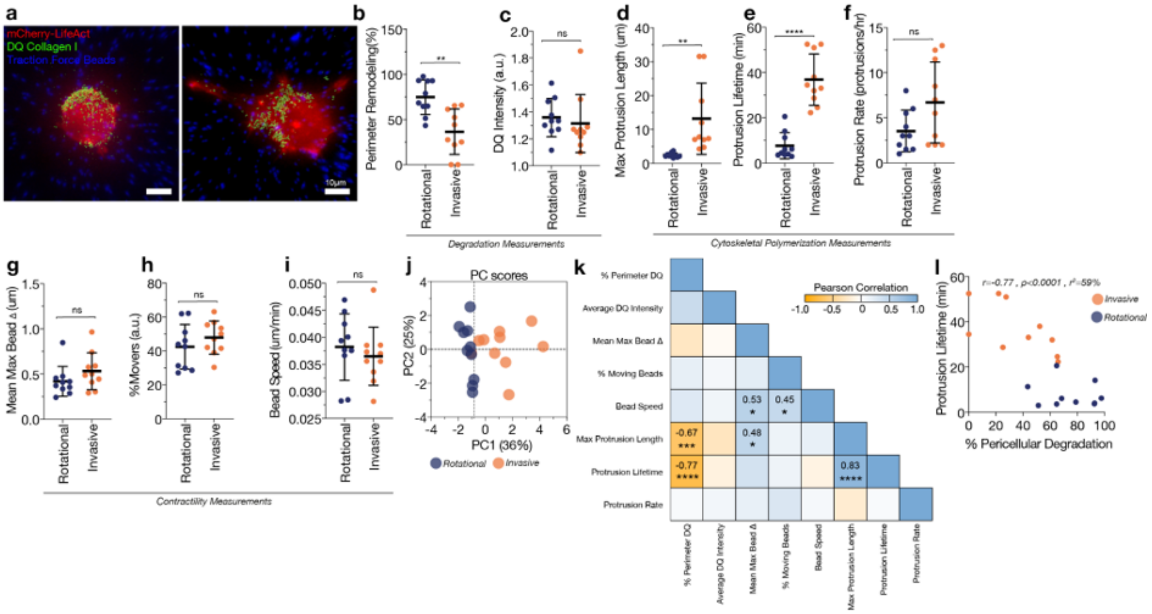

Figure C.1: Experimental data quantification of degradation, cytoskeletal polymerization and contractility measurements. (a): Images showing the actin polymerization (red), ECM degradation signal (green) and traction force bead (blue). (b-c): Degradation measurements based on DQ Collagen I signals. (d-f): Cytoskeletal polymerization measurements based on actin activity. (g-i): Contractility measurements based on movements of traction force beads. (j): Principle components from PCA using the measurement quantities in (b-i) to separate the two phenotypes. (k): Correlations between different pairs of measured quantities. (l): The two phenotypes showed a well-separated linear distribution in the % pericellular degradation (x) and protrusion lifetime (y) phase space.

of 100 μg/mL. Lastly, the cell-buffer solution was mixed into rat tail type I collagen in acetic acid (Corning, Corning, NY) to reach the desired final concentration of 6 mg/mL. The pH was adjusted to 7.0 using 1 N sodium hydroxide and the cell-gel solution was added to custom made PDMS wells mounted on glass bottom dishes (Fluorodish, World Precision Instruments, Sarasota, FL) following thorough mixing. Gels were polymerized at 37 degrees Celsius in a humidified incubator for at least 30 minutes prior to covering the gel with culture medium.

C.3.2 Biophysical Imaging

After 33-39 hours in culture, cells were transferred to a microscope stage top incubator on a Nikon Ti-Eclipse Epifluorescent Inverted Microscope. Multichannel Z-stacks with an axial displacement of 37 μm (1 μm stepsize) were acquired every 2 minutes for 2 hours using an oil-immersion 40x objective (NA 1.5). For each time interval, z-stacks through the cell body were taken in three channels (blue, green, and red), to visualize the fluorescent beads, DQ collagen, and mCherry-LifeAct, respectively. Invasive and rotational cells at the single- to four-cell stage whose primary axis of spreading was along the XY plane were selected for quantitation. Maximum intensity projections (MIPs) of the z-stacks were generated for each time point to generate 2D time series for each channel of the cell selected for analysis.

C.3.3 Biophysical Imaging Analysis

Multichannel z-stacks and MIPs were saved as .tif files and opened in ImageJ for processing and analysis (NIH, Bethesda, MA).

C.3.4 Quantification of Protrusion Dynamics

For cell protrusion dynamics analysis, protrusions were manually tracked in ImageJ using MIP time series of the mCherry-LifeAct expressing cells. In order to determine the Methods 3 time duration or protrusion lifetime, each protrusion was tracked frame-by-frame from initial protrusion extension to complete protrusion retraction. Protrusions longer than 2 μm were included in analysis. The mean protrusion lifetime, length, and rate was calculated for each cell.

C.3.5 Quantification of Matrix Remodeling

In order to quantify the degree of collagen degradation, the fluorescence intensity of a 5 μm band surrounding the cell was measured at each time frame for each slice of the zstack. The total fluorescence intensity values were summed and divided by the total area of the band in order to get mean fluorescence intensity. This value was divided by the mean fluorescence intensity of the background to get the Signal/ Background ratio, referred to as DQ Intensity. To determine the localization of matrix remodeling, binary masks of MIPs of the DQ channel at the first timepoint (t = 1/61) were generated by applying a binary threshold to distinguish signal from background. Next, 1 μm bands along the cell perimeter were generated from MIPs of the cell channel. Lastly, the percent of the band area covered by DQ signal was determined using the Area Fraction measurement in ImageJ. This measurement is referred to as the "Perimeter Remodeling (%)".

C.3.6 Quantification of Traction Force Microscopy Beads

Bead tracking was done using MIPs of the blue channel using the Mosaic plugin in ImageJ. The resulting table containing XY coordinates for each bead in the 165μmx165μm field of view for each timepoint was saved and analyzed using a custom MATLAB script that identifies beads that moved during time-lapse imaging. First, a filter was applied to only analyze the trajectories of beads that were tracked at all time points. After filtering, the displacement at each time point from the initial point was determined for each bead. In order to distinguish beads that were actively being pulled from those moving due to Brownian motion, a moving standard deviation approach was employed. The trajectories of beads not removed by filtering were measured resulting in the mean instantaneous bead speed and mean maximum displacement.

C.4 Velocity tracking image acquisition

MDA-MB-231 H2B-LifeAct and SK-HEP-1 H2B-LifeAct cells were embedded in a 6mg/mL Collagen I gel in a glass bottom 48-well plate, polymerized for 30 minutes, and 200μL of culture medium was added on top. The plate was then transferred to a microscope stage top incubator on a Nikon Ti-E inverted microscope and z-stacks with an axial displacement of 35 μm (1.5μm stepsize) were acquired at 40x magnification every 1 hour for 24 hours. Invasive and rotational cells at the two-cell stage were selected for velocity quantification and all dividing cells were excluded, as determined by the H2B-mCherry channel. Velocity analysis was conducted by using Imaris using object tracking and surface rendering in Bitplane Imaris software. Center of mass for calculating angular velocities was determined by surface rendering of the LifeAct-GFP channel.

C.5 Treatment with pharmacological inhibitors

Matrix metalloproteinases were inhibited using broad-spectrum MMP inhibitor Marimastat (Abcam, Cambridge, United Kingdom) at a concentration of 1μM. As a vehicle control, cells were treated with 0.01% dimethyl sulfoxide (Sigma-Aldrich, St. Louis, MO). Pharmacological inhibitor containing medium was refreshed daily.

Table C.1: Model parameters.

Parameter	Value	Parameter	Value
D	0.0005 $\mu m^2 s^{-1}$	λ_p	400
k_d	9.6 $\times 10^{-5} s^{-1}$	λ_{ECM}	25000
k_r	4.44 $\times 10^{-2} s^{-1}$	λ_a	300
k_+	6.4 $\times 10^{-3} s^{-1}$	$J_{c,m}$	400
k_-	1 $\times 10^{-4} s^{-1}$	$J_{c,e}$	330
A	100 μm^2	$J_{c,c}$	300
G_0	0.0216 $\mu m^2 s^{-1}$	Δx	1 μm
		Δt	20 s

Bibliography

[1] Denise J Montell. “Border-cell migration: the race is on”. In: *Nature Reviews Molecular Cell Biology* 4.1 (2003), pp. 13–24.

[2] Jianxin Jiang, Li Li, Yong He, and Min Zhao. “Collective cell migration: Implications for wound healing and cancer invasion”. In: *Burns Trauma* 1.1 (2013), p. 21. DOI: 10.4103/2321-3868.113331.

[3] Sherry L Murphy, Elizabeth Arias, Jiaquan Xu, and Kenneth D. Kochanek. “Mortality in the United States, 2020”. In: *NCHS Data Brief* no 427 (2021). DOI: 10.15620/cdc:112079.

[4] Andrew G Clark and Danijela Matic Vignjevic. “Modes of cancer cell invasion and the role of the microenvironment”. In: *Current Opinion in Cell Biology* 36 (2015), pp. 13–22. DOI: 10.1016/j.ceb.2015.06.004.

[5] Shuvasree SenGupta, Carole A. Parent, and James E. Bear. “The principles of directed cell migration”. In: *Nature Reviews Molecular Cell Biology* 22.8 (2021), pp. 529–547. DOI: 10.1038/s41580-021-00366-6.

[6] Peter Friedl and Katarina Wolf. “Plasticity of cell migration: A multiscale tuning model”. In: *Journal of Cell Biology* 188.1 (2009), pp. 11–19. DOI: 10.1083/jcb.200909003.

[7] M Abercrombie. “The Croonian Lecture, 1978 - the crawling movement of Metazoan Cells”. In: *Proceedings of the Royal Society of London. Series B. Biological Sciences* 207.1167 (1980), pp. 129–147. DOI: 10.1098/rspb.1980.0017.

[8] Ewa K Paluch and Erez Raz. “The role and regulation of Blebs in cell migration”. In: *Current Opinion in Cell Biology* 25.5 (2013), pp. 582–590. DOI: 10.1016/j.ceb.2013.05.005.

[9] Kota Miura and Florian Siegert. “Light affects camp signaling and cell movement activity in dictyostelium discoideum”. In: *Proceedings of the National Academy of Sciences* 97.5 (2000), pp. 2111–2116. DOI: 10.1073/pnas.040554497.

[10] Athanasius F.M Marée, Alexander V Panfilov, and Paulien Hogeweg. “Migration and thermotaxis of Dictyostelium discoideum slugs, a model study”. In: *Journal of Theoretical Biology* 199.3 (1999), pp. 297–309. DOI: 10.1006/jtbi.1999.0958.

[11] J. T. Bonner, A. Hay, D. G. John, and H. B. Suthers. “Ph affects fruiting and slug orientation in dictyostelium discoideum”. In: *Development* 87.1 (1985), pp. 207–213. DOI: 10.1242/dev.87.1.207.

[12] John ME Nichols, Douwe Veltman, and Robert R Kay. “Chemotaxis of a model organism: Progress with dictyostelium”. In: *Current Opinion in Cell Biology* 36 (2015), pp. 7–12. DOI: 10.1016/j.ceb.2015.06.005.

[13] Salvatore Bozzaro. “The model organism dictyostelium discoideum”. In: *Methods in Molecular Biology* (2013), pp. 17–37.

[14] Pablo A. Iglesias and Peter N. Devreotes. “Navigating through models of chemotaxis”. In: *Curr Opin Cell Biol* 20.1 (2008), pp. 35–40.

[15] Herbert Levine, David A. Kessler, and Wouter-Jan Rappel. “Directional Sensing in eukaryotic chemotaxis: A balanced inactivation model”. In: *Proceedings of the National Academy of Sciences* 103.26 (2006), pp. 9761–9766. DOI: 10.1073/pnas.0601302103.

[16] Carole A Parent and Peter N Devreotes. “A cell’s sense of direction”. In: *Science* 284.5415 (1999), pp. 765–770.

[17] H. Meinhardt. “Orientation of chemotactic cells and growth cones: Models and mechanisms”. In: *Journal of Cell Science* 112.17 (1999), pp. 2867–2874. DOI: 10.1242/jcs.112.17.2867.

[18] Atsuo T. Sasaki, Chris Janetopoulos, Susan Lee, Pascale G. Charest, Kosuke Takeda, Lauren W. Sundheimer, Ruedi Meili, Peter N. Devreotes, and Richard A. Firtel. “G protein–independent Ras/PI3K/F-actin circuit regulates basic cell motility”. In: *Journal of Cell Biology* 178.2 (2007), pp. 185–191. DOI: 10.1083/jcb.200611138.

[19] A.J. Durston. “Dictyostelium discoideum aggregation fields as excitable media”. In: *Journal of Theoretical Biology* 42.3 (1973), pp. 483–504. DOI: 10.1016/0022-5193(73)90242-7.

[20] T. Höfer, J. A. Sherratt, and P. K. Maini. “dictyostelium discoideum: Cellular self-organization in an excitable biological medium”. In: *Proceedings of the Royal Society of London. Series B: Biological Sciences* 259.1356 (1995), pp. 249–257. DOI: 10.1098/rspb.1995.0037.

[21] Monica Skoge, Haicen Yue, Michael Erickstad, Albert Bae, Herbert Levine, Alex Groisman, William F Loomis, and Wouter-Jan Rappel. “Cellular memory in eukaryotic chemotaxis”. In: *Proc Natl Acad Sci U S A* 111.40 (2014), pp. 14448–53. DOI: 10.1073/pnas.1412197111.

[22] Eirikur Palsson, Kyoung J. Lee, Raymond E. Goldstein, Jakob Franke, Richard H. Kessin, and Edward C. Cox. “Selection for spiral waves in the socialamoebae dictyostelium”. In:

Proceedings of the National Academy of Sciences 94.25 (1997), pp. 13719–13723. DOI: 10.1073/pnas.94.25.13719.

[23] Evanthia T Roussos, John S Condeelis, and Antonia Patsialou. “Chemotaxis in cancer”. In: *Nature Reviews Cancer* 11.8 (2011), p. 573.

[24] Marco Baggiolini. “Chemokines and leukocyte traffic”. In: *Nature* 392.6676 (1998), p. 565.

[25] Anne J Ridley, Martin A Schwartz, Keith Burridge, Richard A Firtel, Mark H Ginsberg, Gary Borisy, J Thomas Parsons, and Alan Rick Horwitz. “Cell migration: integrating signals from front to back”. In: *Science* 302.5651 (2003), pp. 1704–1709.

[26] Thomas Gregor, Koichi Fujimoto, Noritaka Masaki, and Satoshi Sawai. “The onset of collective behavior in social amoebae”. In: *Science* 328.5981 (2010), pp. 1021–1025.

[27] W Roos, V Nanjundiah, D Malchow, and G Gerisch. “Amplification of cyclic-AMP signals in aggregating cells of Dictyostelium discoideum”. In: *FEBS letters* 53.2 (1975), pp. 139–142.

[28] BM Shaffer. “Secretion of cyclic AMP induced by cyclic AMP in the cellular slime mould Dictyostelium discoideum”. In: *Nature* 255.5509 (1975), p. 549.

[29] Herbert Levine and Wouter-Jan Rappel. “The physics of eukaryotic chemotaxis”. In: *Phys Today* 66.2 (2013). DOI: 10.1063/PT.3.1884.

[30] Herbert Levine, Igor Aranson, Lev Tsimring, and Thai Viet Truong. “Positive genetic feedback governs cAMP spiral wave formation in Dictyostelium”. In: *Proceedings of the National Academy of Sciences* 93.13 (1996), pp. 6382–6386.

[31] Giovanna De Palo, Darvin Yi, and Robert G Endres. “A critical-like collective state leads to long-range cell communication in Dictyostelium discoideum aggregation”. In: *PLoS biology* 15.4 (2017).

[32] Danying Shao, Wouter-Jan Rappel, and Herbert Levine. “Computational model for Cell Morphodynamics”. In: *Physical Review Letters* 105.10 (2010).

[33] Danying Shao, Herbert Levine, and Wouter-Jan Rappel. “Coupling actin flow, adhesion, and morphology in a computational cell motility model”. In: *Proc Natl Acad Sci U S A* 109.18 (2012), pp. 6851–6856.

[34] Wieland Marth and Axel Voigt. “Signaling networks and cell motility: a computational approach using a phase field description”. In: *Journal of mathematical biology* 69.1 (2014), pp. 91–112.

[35] Andre Levchenko and Pablo A. Iglesias. “Models of eukaryotic gradient sensing: application to chemotaxis of amoebae and neutrophils”. In: *Biophys J* 82 (2002), pp. 50–63.

[36] Wouter-Jan Rappel and Herbert Levine. “Receptor noise limitations on chemotactic sensing”. In: *PNAS* 105.49 (2008), pp. 19270–19275.

[37] Wouter-Jan Rappel and Herbert Levine. “Receptor noise and directional sensing in eukaryotic chemotaxis”. In: *Physical review letters* 100.22 (2008), p. 228101.

[38] Jose Negrete Jr, Alain Pumir, Hsin-Fang Hsu, Christian Westendorf, Marco Tarantola, Carsten Beta, and Eberhard Bodenschatz. “Noisy Oscillations in the Actin Cytoskeleton of Chemotactic Amoeba”. In: *Physical review letters* 117.14 (2016), p. 148102.

[39] Hsin-Fang Hsu, Eberhard Bodenschatz, Christian Westendorf, Azam Gholami, Alain Pumir, Marco Tarantola, and Carsten Beta. “Variability and order in cytoskeletal dynamics of motile amoeboid cells”. In: *Physical review letters* 119.14 (2017), p. 148101.

[40] Raymond E Goldstein. “Traveling-wave chemotaxis”. In: *Physical review letters* 77.4 (1996), p. 775.

[41] Akihiko Nakajima, Shuji Ishihara, Daisuke Imoto, and Satoshi Sawai. “Rectified directional sensing in long-range cell migration”. In: *Nature communications* 5 (2014).

[42] Tim Lämmermann, Philippe V Afonso, Bastian R Angermann, Ji Ming Wang, Wolfgang Kastenmüller, Carole A Parent, and Ronald N Germain. “Neutrophil swarms require LTB4 and integrins at sites of cell death in vivo”. In: *Nature* 498.7454 (2013), pp. 371–375.

[43] Bashar Hamza, Elisabeth Wong, Sachin Patel, Hansang Cho, Joseph Martel, and Daniel Irimia. “Retrotaxis of human neutrophils during mechanical confinement inside microfluidic channels”. In: *Integrative Biology* 6.2 (2014), pp. 175–183.

[44] KJ Tomchik and Peter N Devreotes. “Adenosine 3’, 5’-monophosphate waves in Dictyostelium discoideum: a demonstration by isotope dilution–fluorography”. In: *Science* 212.4493 (1981), pp. 443–446.

[45] Sonya Bader, Arjan Kortholt, and Peter JM Van Haastert. “Seven Dictyostelium discoideum phosphodiesterases degrade three pools of cAMP and cGMP”. In: *Biochemical Journal* 402.1 (2007), pp. 153–161.

[46] Paul Herzmark, Kyle Campbell, Fei Wang, Kit Wong, Hana El-Samad, Alex Groisman, and Henry R. Bourne. “Bound attractant at the leading vs. the trailing edge determines chemotactic prowess”. In: *Proceedings of the National Academy of Sciences* 104.33 (2007), pp. 13349–13354. DOI: 10.1073/pnas.0705889104.

[47] Yuhai Tu and Wouter-Jan Rappel. “Adaptation in living systems”. In: *Annual review of condensed matter physics* 9 (2018), pp. 183–205.

[48] Peter N Devreotes, Michael J Potel, and Stephen A MacKay. “Quantitative analysis of cyclic AMP waves mediating aggregation in Dictyostelium discoideum”. In: *Developmental biology* 96.2 (1983), pp. 405–415.

[49] Marten Postma and Peter JM van Haastert. “Mathematics of experimentally generated chemoattractant gradients”. In: *Chemotaxis*. Springer, 2009, pp. 473–488.

[50] Richa Karmakar, Christoph Schich, Nadine Kamprad, Vanessa Scheller, Edgar Gutierrez, Alex Groisman, Wouter-Jan Rappel, and Marco Tarantola. “Novel micropatterning technique reveals dependence of cell-substrate adhesion and migration of social amoebas on parental strain, development, and fluorescent markers”. In: *PloS one* 15.7 (2020), e0236171.

[51] Danny Fuller, Wen Chen, Micha Adler, Alex Groisman, Herbert Levine, Wouter-Jan Rappel, and William F Loomis. “External and internal constraints on eukaryotic chemotaxis”. In: *Proc Natl Acad Sci U S A* 107.21 (2010), pp. 9656–9659.

[52] Maurice Sussman. “Cultivation and synchronous morphogenesis of Dictyostelium under controlled experimental conditions”. In: *Methods in cell biology*. Vol. 28. Elsevier, 1987, pp. 9–29.

[53] Kosuke Takeda, Danying Shao, Micha Adler, Pascale G Charest, William F Loomis, Herbert Levine, Alex Groisman, Wouter-Jan Rappel, and Richard A Firtel. “Incoherent feedforward control governs adaptation of activated ras in a eukaryotic chemotaxis pathway”. In: *Sci. Signal.* 5.205 (2012), ra2–ra2.

[54] L. Bosgraaf and P. J. Van Haastert. “Navigation of chemotactic cells by parallel signaling to pseudopod persistence and orientation”. In: *PLoS ONE* 4.8 (2009), e6842.

[55] Monica Skoge, Micha Adler, Alex Groisman, Herbert Levine, William F Loomis, and Wouter-Jan Rappel. “Gradient sensing in defined chemotactic fields”. In: *Integrative Biology* 2.11-12 (2010), pp. 659–668.

[56] Arpan Bhowmik, Wouter-Jan Rappel, and Herbert Levine. “Excitable waves and direction-sensing in Dictyostelium discoideum: steps towards a chemotaxis model”. In: *Physical biology* 13.1 (2016), p. 016002.

[57] Wouter-Jan Rappel, Alastair Nicol, Armand Sarkissian, Herbert Levine, and William F. Loomis. “Self-organized vortex state in two-dimensionaldictyosteliumdynamics”. In: *Physical Review Letters* 83.6 (1999), pp. 1247–1250. DOI: 10.1103/physrevlett.83.1247.

[58] Masashi Fukuzawa. "Control of prestalk-cell differentiation by transcription factors". In: *Development, Growth and Differentiation* 53.4 (2011), pp. 538–547. DOI: 10.1111/j.1440-169x.2011.01269.x.

[59] Kyogo Kawaguchi, Ryoichiro Kageyama, and Masaki Sano. "Topological defects control collective dynamics in neural progenitor cell cultures". In: *Nature* 545.7654 (2017), pp. 327–331. DOI: 10.1038/nature22321.

[60] Tzer Han Tan, Jinghui Liu, Pearson W. Miller, Melis Tekant, Jörn Dunkel, and Nikta Fakhri. "Topological turbulence in the membrane of a living cell". In: *Nature Physics* 16.6 (2020), pp. 657–662. DOI: 10.1038/s41567-020-0841-9.

[61] Richard J. Field and Maria Burger. *Oscillations and traveling waves in chemical systems*. Wiley, 1985.

[62] Haruki Odaka, Satoshi Arai, Takafumi Inoue, and Tetsuya Kitaguchi. "Genetically-encoded yellow fluorescent camp indicator with an expanded dynamic range for dual-color imaging". In: *PLoS ONE* 9.6 (2014). DOI: 10.1371/journal.pone.0100252.

[63] William Thielicke and Eize J. Stamhuis. "PIVlab – towards user-friendly, affordable and accurate digital particle image velocimetry in Matlab". In: *Journal of Open Research Software* 2 (2014). DOI: 10.5334/jors.bl.

[64] Xavier Trepat, Michael R. Wasserman, Thomas E. Angelini, Emil Millet, David A. Weitz, James P. Butler, and Jeffrey J. Fredberg. "Physical forces during collective cell migration". In: *Nature Physics* 5.6 (2009), pp. 426–430. DOI: 10.1038/nphys1269.

[65] Dhananjay T. Tambe, Ugo Croutelle, Xavier Trepat, Chan Young Park, Jae Hun Kim, Emil Millet, James P. Butler, and Jeffrey J. Fredberg. "Monolayer stress microscopy: Limitations, artifacts, and accuracy of recovered intercellular stresses". In: *PLoS ONE* 8.2 (2013). DOI: 10.1371/journal.pone.0055172.

[66] Hidenori Hashimura, Yusuke V. Morimoto, Masato Yasui, and Masahiro Ueda. "Collective cell migration of dictyostelium without camp oscillations at multicellular stages". In: *Communications Biology* 2.1 (2019). DOI: 10.1038/s42003-018-0273-6.

[67] Richa Karmakar, Man-Ho Tang, Haicen Yue, Daniel Lombardo, Aravind Karanam, Brian A. Camley, Alex Groisman, and Wouter-Jan Rappel. "Cellular memory in eukaryotic chemotaxis depends on the background chemoattractant concentration". In: *Physical Review E* 103.1 (2021). DOI: 10.1103/physreve.103.012402.

[68] Jean-Paul Rieu, Catherine Barentin, Yasuo Maeda, and Yasuji Sawada. "Direct mechanical force measurements during the migration of dictyostelium slugs using flexible substrata". In: *Biophysical Journal* 89.5 (2005), pp. 3563–3576. DOI: 10.1529/biophysj.104.056333.

[69] François Graner and James A. Glazier. “Simulation of biological cell sorting using a two-dimensional extended Potts model”. In: *Physical Review Letters* 69.13 (1992), pp. 2013–2016. DOI: 10.1103/physrevlett.69.2013.

[70] F. Y. Wu. “The potts model”. In: *Reviews of Modern Physics* 54.1 (1982), pp. 235–268. DOI: 10.1103/revmodphys.54.235.

[71] Nicholas J. Savill and Paulien Hogeweg. “Modelling morphogenesis: From single cells to crawling slugs”. In: *Journal of Theoretical Biology* 184.3 (1997), pp. 229–235. DOI: 10.1006/jtbi.1996.0237.

[72] András Szabó and Roeland M. Merks. “Cellular potts modeling of tumor growth, tumor invasion, and tumor evolution”. In: *Frontiers in Oncology* 3 (2013). DOI: 10.3389/fonc.2013.00087.

[73] Vladimir P. Zhdanov and Bengt Kasemo. “Simulation of the growth and differentiation of stem cells on a heterogeneous scaffold”. In: *Physical Chemistry Chemical Physics* 6.17 (2004), p. 4347. DOI: 10.1039/b407371c.

[74] Marco Scianna. “An extended cellular Potts model analyzing a wound healing assay”. In: *Computers in Biology and Medicine* 62 (2015), pp. 33–54. DOI: 10.1016/j.compbiomed.2015.04.009.

[75] Noriyuki Bob Ouchi, James A. Glazier, Jean-Paul Rieu, Arpita Upadhyaya, and Yasuji Sawada. “Improving the realism of the cellular Potts model in simulations of biological cells”. In: *Physica A: Statistical Mechanics and its Applications* 329.3-4 (2003), pp. 451–458. DOI: 10.1016/s0378-4371(03)00574-0.

[76] Shreyansh Jain, Victoire M. Cachoux, Gautham H. Narayana, Simon de Beco, Joseph D’Alessandro, Victor Cellerin, Tianchi Chen, Mélina L. Heuzé, Philippe Marcq, René-Marc Mège, and et al. “The role of single-cell mechanical behaviour and polarity in driving collective cell migration”. In: *Nature Physics* 16.7 (2020), pp. 802–809. DOI: 10.1038/s41567-020-0875-z.

[77] M. Reffay, L. Petitjean, S. Coscoy, E. Grasland-Mongrain, F. Amblard, A. Buguin, and P. Silberzan. “Orientation and polarity in collectively migrating cell structures: Statics and dynamics”. In: *Biophysical Journal* 100.11 (2011), pp. 2566–2575. DOI: 10.1016/j.bpj.2011.04.047.

[78] Clare M. Waterman-Storer, Rebecca A. Worthylake, Betty P. Liu, Keith Burridge, and E.D. Salmon. “Microtubule growth activates RAC1 to promote lamellipodial protrusion in fibroblasts”. In: *Nature Cell Biology* 1.1 (1999), pp. 45–50. DOI: 10.1038/9018.

[79] Matthias Schaks, Grégory Giannone, and Klemens Rottner. “Actin dynamics in cell migration”. In: *Essays in Biochemistry* 63.5 (2019), pp. 483–495. DOI: 10.1042/ebc20190015.

[80] Richard FitzHugh. “Mathematical models of threshold phenomena in the nerve membrane”. In: *The Bulletin of Mathematical Biophysics* 17.4 (1955), pp. 257–278. DOI: 10.1007/bf02477753.

[81] Elisabeth G. Rens and Leah Edelstein-Keshet. “From energy to cellular forces in the cellular potts model: An algorithmic approach”. In: *PLOS Computational Biology* 15.12 (2019). DOI: 10.1371/journal.pcbi.1007459.

[82] Bakthier Vasiev, Florian Siegert, and Cornelis Weijer. “Multiarmed spirals in excitable media”. In: *Physical Review Letters* 78.12 (1997), pp. 2489–2492. DOI: 10.1103/physrevlett.78.2489.

[83] Bin Wang and Adam Kuspa. “dictyostelium development in the absence of Camp”. In: *Science* 277.5323 (1997), pp. 251–254. DOI: 10.1126/science.277.5323.251.

[84] Ilan Spector, Nava R. Shochet, Yoel Kashman, and Amiram Groweiss. “Latrunculins: Novel marine toxins that disrupt Microfilament organization in cultured cells”. In: *Science* 219.4584 (1983), pp. 493–495. DOI: 10.1126/science.6681676.

[85] Gail Singer, Tsuyoshi Araki, and Cornelis J. Weijer. “Oscillatory camp cell-cell signalling persists during multicellular Dictyostelium development”. In: *Communications Biology* 2.1 (2019). DOI: 10.1038/s42003-019-0371-0.

[86] FLORIAN SIEGERT and CORNELIS WEIJER. “Digital image processing of optical density wave propagation in dictyostelium discoideum and analysis of the effects of caffeine and ammonia”. In: *Journal of Cell Science* 93.2 (1989), pp. 325–335. DOI: 10.1242/jcs.93.2.325.

[87] Fumihito Fukujin, Akihiko Nakajima, Nao Shimada, and Satoshi Sawai. “Self-organization of chemoattractant waves indictyosteliumdepends on F-actin and cell–substrate adhesion”. In: *Journal of The Royal Society Interface* 13.119 (2016), p. 20160233. DOI: 10.1098/rsif.2016.0233.

[88] V. S. Zykov. “Spiral wave initiation in excitable media”. In: *Philosophical Transactions of the Royal Society A: Mathematical, Physical and Engineering Sciences* 376.2135 (2018), p. 20170379. DOI: 10.1098/rsta.2017.0379.

[89] Andrew H. Beck, Ankur R. Sangoi, Samuel Leung, Robert J. Marinelli, Torsten O. Nielsen, Marc J. van de Vijver, Robert B. West, Matt van de Rijn, and Daphne Koller. “Systematic analysis of breast cancer morphology uncovers stromal features associated with survival”. In: *Science Translational Medicine* 3.108 (2011). DOI: 10.1126/scitranslmed.3002564.

[90] Jinru Shia, Nikolaus Schultz, Deborah Kuk, Efsevia Vakiani, Sumit Middha, Neil H Segal, Jaclyn F Hechtman, Michael F Berger, Zsofia K Stadler, Martin R Weiser, and et al. “Morphological characterization of colorectal cancers in the cancer genome atlas reveals

distinct morphology–molecular associations: Clinical and biological implications". In: *Modern Pathology* 30.4 (2016), pp. 599–609. DOI: 10.1038/modpathol.2016.198.

[91] Pahini Pandya, Jose L. Orgaz, and Victoria Sanz-Moreno. "Modes of invasion during tumour dissemination". In: *Molecular Oncology* 11.1 (2016), pp. 5–27. DOI: 10.1002/1878-0261.12019.

[92] Agata Jabłońska-Trypuć, Marzena Matejczyk, and Stanisław Rosochacki. "Matrix metalloproteinases (mmps), the main extracellular matrix (ECM) enzymes in collagen degradation, as a target for anticancer drugs". In: *Journal of Enzyme Inhibition and Medicinal Chemistry* 31.sup1 (2016), pp. 177–183. DOI: 10.3109/14756366.2016.1161620.

[93] Marie-Pia d'Ortho, Heather Stanton, Michael Butler, Susan J Atkinson, Gillian Murphy, and Rosalind M Hembry. "MT1-MMP on the cell surface causes focal degradation of gelatin films". In: *FEBS Letters* 421.2 (1998), pp. 159–164. DOI: 10.1016/s0014-5793(97)01555-x.

[94] Ilya Ulasov, Bart Thaci, Purvaba Sarvaiya, Ruiyang Yi, Donna Guo, Brenda Auffinger, Peter Pytel, Lingjiao Zhang, Chung Kwon Kim, Anton Borovjagin, and et al. "Inhibition of mmp 14 potentiates the therapeutic effect of temozolomide and radiation in gliomas". In: *Cancer Medicine* 2.4 (2013), pp. 457–467. DOI: 10.1002/cam4.104.

[95] Olaf Ronneberger, Philipp Fischer, and Thomas Brox. "U-net: Convolutional networks for biomedical image segmentation". In: *International Conference on Medical image computing and computer-assisted intervention*. Springer. 2015, pp. 234–241.